### **OPEN ACCESS**



# An Image-based Search for Pulsar Candidates in the MeerKAT Bulge Survey

Dale A. Frail , Emil Polisensky , Scott D. Hyman , William D. Cotton , Namir E. Kassim , Michele L. Silverstein , Rahul Sengar , David L. Kaplan , Francesca Calore , Joanna Berteaud , Marica Clavel , Marica Geyer , Rahul Sengar , David L. Kaplan , Francesca Calore , Joanna Berteaud , Marica Clavel , Marica Geyer , National Radio Astronomy Observatory, P.O. Box O, Socorro, NM 87801, USA; dfrail@nrao.edu , V.S. Naval Research Laboratory, 4555 Overlook Ave. SW, Washington, DC 20375, USA , Department of Engineering and Physics, Sweet Briar College, Sweet Briar, VA 24595, USA , National Radio Astronomy Observatory, 520 Edgemont Road, Charlottesville, VA 22903, USA , National Radio Astronomy Observatory, 520 Edgemont Road, Charlottesville, VA 22903, USA , National Radio Astronomy Observatory, Suniversity of Wisconsin–Milwaukee, PO Box 413, Milwaukee, WI 53201, USA , Laboratoire d'Annecy-le-Vieux de Physique Théorique, CNRS, F-74000 Annecy, France , University of Maryland, Department of Astronomy, College Park, MD 20742, USA , NASA Goddard Space Flight Center, Code 662, Greenbelt, MD 20771, USA , Université Grenoble Alpes, CNRS, IPAG, F-38000 Grenoble, France , University of Cape Town, Rondebosch 7701, South Africa

### Abstract

We report on the results of an image-based search for pulsar candidates toward the Galactic bulge. We used mosaic images from the MeerKAT radio telescope that were taken as part of a  $173 \, \mathrm{deg^2}$  survey of the bulge and Galactic center of our Galaxy at L band (856–1712 MHz) in all four Stokes I, Q, U, and V. The image rms noise levels of 12– $17 \, \mu\mathrm{Jy}$  ba $^{-1}$  represent a significant increase in sensitivity over past image-based pulsar searches. Our primary search criterion was circular polarization, but we used other criteria, including linear polarization, in-band spectral index, compactness, variability, and multiwavelength counterparts to select pulsar candidates. We first demonstrate the efficacy of this technique by searching for polarized emission from known pulsars and comparing our results with measurements from the literature. Our search resulted in a sample of 75 polarized sources. Bright stars or young stellar objects were associated with 28 of these sources, including a small sample of highly polarized dwarf stars with pulsar-like steep spectra. Comparing the properties of this sample with the known pulsars, we identified 30 compelling candidates for pulsation follow-up, including two sources with both strong circular and linear polarization. The remaining 17 sources are either pulsars or stars, but we cannot rule out an extragalactic origin or image artifacts among the brighter, flat-spectrum objects.

*Unified Astronomy Thesaurus concepts*: Galactic radio sources (571); Polarimetry (1278); High energy astrophysics (739); Spectral index (1553); Extragalactic radio sources (508); Radio pulsars (1353); Radio continuum emission (1340)

#### 1. Introduction

With the advent of a new generation of sensitive wide-field radio interferometers, there has been a renewed interest in imaging the Galactic center (GC) and the bulge of our Galaxy (I. Heywood et al. 2022; Z. Wang et al. 2022b; S. Goedhart et al. 2024). Early pioneering efforts revealed a significant population of compact radio sources (T. N. LaRosa et al. 2000; M. E. Nord et al. 2004; T. J. W. Lazio & J. M. Cordes 2008), while time-domain monitoring led to the discovery of new classes of transients and variable objects (e.g., J.-H. Zhao et al. 1992; S. D. Hyman et al. 2005; Z. Wang et al. 2021; J.-H. Zhao et al. 2022).

Another important application of image-based radio surveys is the identification of pulsar candidates (e.g., D. L. Kaplan et al. 2000; F. de Gasperin et al. 2018). It has long been argued that the enhanced stellar densities in the GC and Galactic bulge

Original content from this work may be used under the terms of the Creative Commons Attribution 4.0 licence. Any further distribution of this work must maintain attribution to the author(s) and the title of the work, journal citation and DOI.

could lead to a significant number of pulsars, and in particular millisecond pulsars (MSPs; M. P. Muno et al. 2006; J.-P. Macquart & N. Kanekar 2015; J. Berteaud et al. 2021). There is an ongoing debate on whether the diffuse gamma-ray emission from the Galactic bulge, the so-called gamma-ray excess identified by the Fermi Large Area Gamma-Ray Telescope, originates from a population of thousands of (or more) MSPs or is the first nongravitational signature of dark matter particle annihilation (e.g., F. Calore et al. 2021; D. Song et al. 2024; see S. Murgia 2020 for a review). Identifying pulsations from this putative MSP population would go a long way in resolving this controversy, but the existing census of pulsars is inadequate (F. Calore et al. 2016). Traditional pulsation searches suffer from a number of special challenges in this direction (F. Calore et al. 2016), but they can be effective when used together with image-based methods (D. A. Frail et al. 2018; R. Anna-Thomas et al. 2024; A. V. McCarver et al. 2024; Z. Wang et al. 2024), as well as when combined with multiwavelength cross-correlations (J. Berteaud et al. 2023).

The initial image-based pulsar searches in the Galactic bulge and GC relied on only two pulsar properties: their compactness and steep spectral indices (D. Bhakta et al. 2017; S. D. Hyman et al. 2019). Variability has been rediscovered as a sufficient but

South African Radio Astronomy Observatory, 2 Fir Street, Black River Park, Observatory 7925, South Africa Received 2024 June 12; revised 2024 August 12; accepted 2024 August 27; published 2024 October 23

<sup>&</sup>lt;sup>12</sup> NRC Research Associate.

not necessary condition for identifying promising pulsar candidates (Z. Wang et al. 2022b; I. Heywood 2023; S. Sett et al. 2023), but polarization has proven to be an even more powerful search criterion. Pulsars appear to be unique among compact radio sources for having both steep spectra and high degrees of linear and/or circular polarization (S. Johnston & M. Kerr 2018; C. Sobey et al. 2021). Identifying pulsar candidates by a high degree of polarization in the image plane was first used to identify the young, energetic pulsar PSR B1951 +32 in the supernova remnant CTB 80 (R. G. Strom 1987), and then again to identify the luminous MSP PSR J0218+4232 (J. Navarro et al. 1995). Recently there has been a resurgence in imaging surveys with an emphasis on polarization (E. Lenc et al. 2018; C. Sobey et al. 2022; Y. Wang et al. 2022a; J. R. Callingham et al. 2023; S. W. Duchesne et al. 2023). There has been some initial success at identifying promising pulsar candidates in the GC and bulge using polarization as an additional search criterion (S. D. Hyman et al. 2021; Y. Wang et al. 2022a; Z. Wang et al. 2022b).

In this paper we build on these efforts by using a new sensitive survey of the Galactic bulge and GC region in full Stokes in a search for pulsar candidates. The paper is organized as follows: We present the data analyzed and data reduction pipeline in Sections 2 and 3, respectively. In Section 4, we illustrate the method followed to build our main source catalog, including a discussion of survey properties and known data issues. In Section 5, we put forward our selection strategy for pulsar candidates, mainly based on polarization characteristics. In Section 6, we comment on other important selection criteria. The main results are presented in Section 7, where we present the pulsar candidate list and a detailed discussion about the nondetection of some of these in previous pulsation search campaigns. We conclude in Section 8.

#### 2. Observations

For this work we have used an archival South African Radio Astronomy Observatory (SARAO) Legacy Survey of the Galactic Center Region (Code SSV-20180505-FC-01), taken with the 64-element MeerKAT Radio Telescope array (J. Jonas & MeerKAT Team 2016; F. Camilo et al. 2018; T. Mauch et al. 2020). A vertical strip at approximately  $|b| < 20^{\circ}$  and at least  $|l| < 1^{\circ}$ 5 (widening to  $\pm 4.^{\circ}$ 5 at lower latitudes) was observed toward the GC, using the *L*-band receivers (856–1712 MHz). A total of 315 individual pointings were made during 42 sessions from 2019 December 26 to 2020 August 5. A single session was typically 8–10 hr in duration, during which seven or eight pointings were observed, each receiving approximately 1 hr in total integration time. Pointings were widely spaced in hour angle to maximize spatial frequency (uv) coverage.

The MeerKAT correlator was configured to produce 4096 channels across the full bandwidth in 8 s sampling in all four combinations (XX, YY, XY, and YX) of the orthogonal linearly polarized feeds. PKS B1934–638 was used as the photometric and bandpass calibrator, 3C 286 was used as the polarization calibrator, and a nearby astrometric calibrator was used for each session. For a similar observational setup see I. Heywood et al. (2022), or consult the MeerKAT Knowledge Base <sup>13</sup> for current best practices.

**Table 1**Observational Properties of Bulge Mosaics

l (deg)	b (deg)	No. of Sources	rms (μJy ba <sup>-1</sup> )	Known PSRs	Candi. (V, P)
0.000	+17.5	21,532	14.6	1	1, 0
0.000	+14.5	23,088	13.9	1	0, 0
0.000	+11.5	17,287	16.9	0	2, 1
0.000	+8.5	17,966	17.7	2	3, 1
003.0	+5.5	15,819	16.0	4	1, 2
357.0	+5.5	13,367	17.4	3	4, 0
0.000	+5.5	25,086	12.5	4	7, 0
003.0	+2.5	17,769	14.7	7	2, 0
357.0	+2.5	14,261	15.3	9	0, 1
0.000	+2.5	18,815	14.3	10	4, 2
0.000	-2.5	19,709	14.0	18	6, 0
357.0	-2.5	14,451	14.7	7	3, 0
003.0	-2.5	12,715	16.8	11	4, 0
0.000	-5.5	29,992	10.7	4	1, 0
357.0	-5.5	22,252	11.9	5	3, 0
003.0	-5.5	21,019	11.9	2	3, 0
0.000	-8.5	23,350	13.4	0	6, 4
0.000	-11.5	20,847	13.5	1	4, 1
0.000	-14.5	27,358	11.4	0	4, 0
0.000	-17.5	26,322	12.1	1	9, 0

#### 3. Data Reduction

All calibration, imaging, and mosaicking were carried out in the Obit software package <sup>14</sup> following standard procedures. We summarize this process here, but a full description is given in the recently released SARAO MeerKAT 1.3 GHz Galactic Plane Survey (S. Goedhart et al. 2024).

Calibration and editing followed procedures established by T. Mauch et al. (2020), in which instrumental data errors and radio interference were identified and flagged. The data were then calibrated for phase, amplitude, bandpass, and group delays as described by K. Knowles et al. (2022). Polarization calibration followed the same procedure outlined in S. Goedhart et al. (2024), using 3C 286 as a polarized calibrator and PKS B1934–638 as an unpolarized source.

Once calibrated the individual pointings in all four Stokes I, Q, U, and V were imaged and deconvolved within Obit. These individual pointings were formed into 20 partially overlapping linear mosaics each  $3^{\circ}.125 \times 3^{\circ}.125$  in size using the optimal weighting scheme described in S. Goedhart et al. (2024). Each mosaic was also imaged in 14 subbands, with bandwidths ranging from 43 to 74 MHz. However, the middle two subbands were severely affected by radio frequency interference (RFI) and had to be discarded. As a result, there are six good subband images that span frequencies from 886 to 1171 MHz and another six that span frequencies from 1286 to 1681 MHz.

The 20 different mosaic fields given in the Galactic coordinate system (l, b), along with their properties, are shown in Table 1 and plotted in Figure 1. In Figure 2 we show an example of the Stokes I (left) and Stokes V (right) mosaic images for the G0.0+5.5 pointing.

### 4. Source Catalog

For the source catalog and the following analysis we used a preliminary version of the mosaic images. For the entire survey, including full Stokes mosaic images and a gallery of

<sup>13</sup> https://skaafrica.atlassian.net/wiki/spaces/ESDKB/overview?homepageId=41025669

<sup>14</sup> http://www.cv.nrao.edu/~bcotton/Obit.html

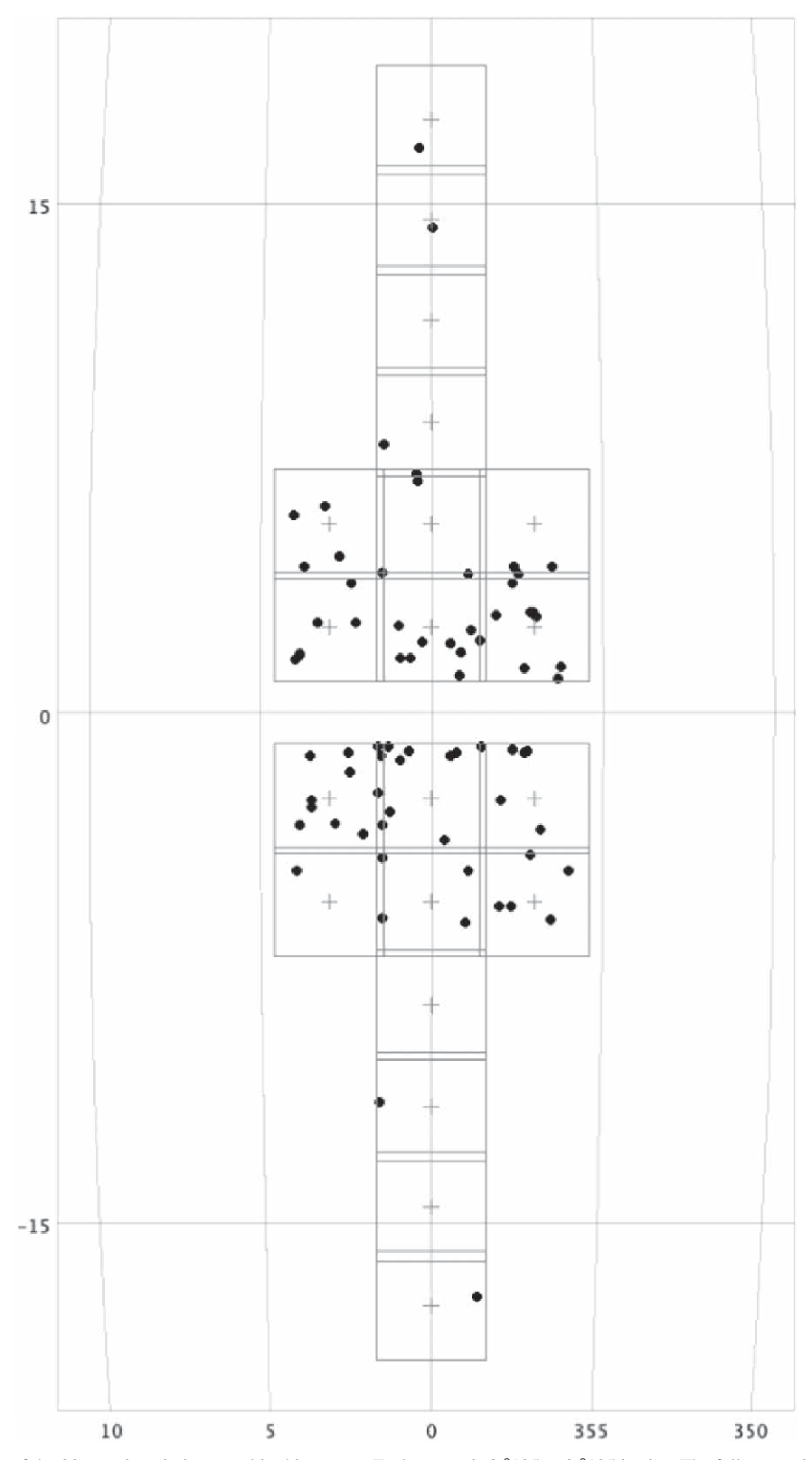


Figure 1. Galactic distribution of the 20 mosaic pointings used in this survey. Each square is  $3.^{\circ}125 \times 3.^{\circ}125$  in size. The full survey is symmetric about the GC and covers a vertical strip  $\pm 20^{\circ}$  in latitude and at least  $\pm 1.^{\circ}5$  in longitude, but it widens to  $\pm 4.^{\circ}5$  at lower latitudes. The positions of the known pulsars that lie within the survey area are indicated by filled circles.

extended sources, we refer the reader to W. D. Cotton & SARAO Meerkat Bulge Survey Team (2024, in preparation). As our primary scientific goal is producing a list of pulsar candidates, the following discussions on source catalogs, their

properties, and any data issues are focused on unresolved point sources.

We utilized PyBDSF (N. Mohan & D. Rafferty 2015) to generate source catalogs for all images. PyBDSF subtracts a

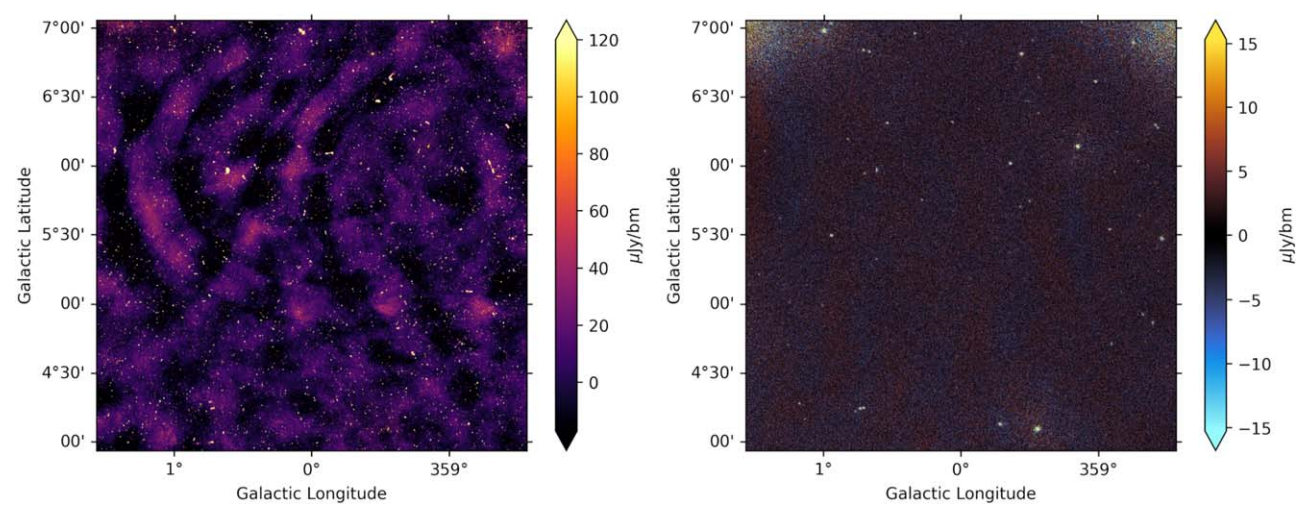


Figure 2. A typical  $3^{\circ}.125 \times 3^{\circ}.125$  mosaic field for one of the 20 pointings. These are Stokes I (left) and Stokes V (right) images for the G0.0+5.5 mosaic field. There are approximately 25,000 radio continuum sources. After eliminating image artifacts and other false positives (see Section 5), we identify four known pulsars and seven circularly polarized sources but no linearly polarized sources in this mosaic field.

mean background map from the pixel intensities and normalizes each pixel value to the local noise, which is determined through interpolation from a coarsely sampled grid. Extensive testing showed that a grid sampling of 25 pixels provides robust background subtraction and source flux measurements. The mean pixel intensity and standard deviation are calculated within a square box of 75 pixels on a side centered at each grid point. Pixels belonging to sources are excluded from the background calculation by iteratively rejecting outliers with large positive values. Islands of connected pixels that exceed 3 times the local noise are used to define sources, with elliptical Gaussian fitting initiated at the locations of pixel peaks within these islands. Sources with a signal-to-noise ratio (S/N) < 5 and sources within 10 pixels of the image borders are discarded. We use the source catalogs of combined Gaussian components to separate multicomponent from single-component sources, a characteristic of unresolved point sources. Negative polarizations were cataloged by running PyBDSF on the negated Stokes Q, U, and V images.

Linear polarization images were created for each subband  $(P = \sqrt{Q^2 + U^2})$  and for the full bandwidth by averaging P over all subbands. Additionally, half bandwidth and quarter bandwidth images were constructed by averaging subbands in groups of six and three, respectively, for all polarizations. Source spectra  $(S_{\nu} \propto \nu^{\alpha})$  were independently determined in the half-band, quarter-band, and subband images through inversevariance-weighted fits to sources detected more than once. Note that we neglected to correct our linear polarization images for noise bias (S. J. George et al. 2012). Originally we intended to focus our efforts exclusively on finding circularly polarized sources, but in the spirit of investigating the full capabilities of this data set, we decided to add linearly polarized searches. The lessons learned from this pilot effort, including the impact of neglecting the noise bias, are discussed in more detail in Sections 5.1 and 5.3.

The presence of blanked regions in the mosaic subbands complicates determining source spectra in the half- and quarter-band images. At lower frequencies, these blanked regions are randomly distributed across the field owing to the need for RFI flagging of entire pointings. At higher frequencies, the field of view is smaller, and blanking tends to occur near the mosaic

edges. To account for this, we calculated the average frequency across the subband-combined images, excluding the blanked regions. We then used these position-dependent frequencies for fitting source spectra.

The full bandwidth mosaic's Stokes I catalog serves as the foundation for the complete source catalog in each field. Polarized sources were identified by locating the nearest source within 8'' in the polarization catalogs. Spectral indices were assigned by matching the full bandwidth catalog to the halfband, quarter-band, and subband source catalogs.

To classify sources as compact or extended, we adopt the popular method (e.g., H. T. Intema et al. 2017; F. de Gasperin et al. 2018) analyzing the total-to-peak flux ratio (R) of single-component sources binned by S/N for each field catalog. We calculate the average and standard deviation of R within each bin after iteratively removing  $2\sigma$  outliers to exclude extended sources. We then fit a smoothly varying function of S/N to the  $+2\sigma$  envelope using an empirical equation adapted from W. L. Williams et al. (2013). We defined a compactness metric as the ratio of R obtained from the fitted equation to the value measured for the source, serving as a statistical measure of source extent. Single-component sources with a compactness greater than 1 have a  $\sim$ 97% probability of being unresolved.

# 4.1. Survey Properties

Table 1 displays the number of sources in each field catalog. By associating sources within  $8^{\prime\prime}$  across different fields, we identified 387,875 unique sources within the 173 deg² survey area. Among these, 375,286 are classified as single component, with 298,785 being unresolved (compactness > 1). A total of 188,753 sources lack in-band spectral index determinations. For circularly polarized sources without spectral indices (Section 5.2), we utilize PyBDSF in forced-fitting mode, where the full-band source position is used to initiate Gaussian fitting in the individual subbands and subband combination images, enabling spectral indices to be obtained with flux measurements of weaker detections (S/N > 3).

The number of International Celestial Reference Frame (ICRF; P. Charlot et al. 2020) sources within our survey area is insufficient for direct astrometric correction calculation. To tackle this issue, we employed a two-step correction process.

First, we corrected each field to the RACS-mid catalog (S. W. Duchesne et al. 2023), utilizing the median offset of unresolved sources isolated from their nearest neighbors by at least 16" and within 8" of an unresolved RACS-mid source. We achieved 235–369 matches per field, with median offsets and standard deviations of  $\Delta\alpha$  cos  $\delta$ = (-0."33 to 1."02)  $\pm$  (0."50–0."85) and  $\Delta\delta$  = (-0."53 to 1."43)  $\pm$  (0."43–0."92). The astrometric offset magnitudes are less than 1 pixel for all fields. Second, we determined the correction to ICRF using the offset of unresolved RACS-mid sources within 8" of ICRF sources. To account for potential systematic effects, we limited our calculation to RACS-mid sources within 40° of the GC. From 134 matches, we obtained  $\Delta\alpha$  cos $\delta$  = -0."21  $\pm$  0."35 and  $\Delta\delta$  = 0."10  $\pm$  0."31. These offsets are within 1 $\sigma$  of those calculated for the entire catalog (S. W. Duchesne et al. 2023).

Figure 3 shows the offset distribution for all 6766 sources with RACS-mid matches, after correcting for the median offset. The standard deviation is 0."65 in both coordinates for the entire sample.

### 4.2. Known Data Issues

These data were taken during an active development and commissioning stage of MeerKAT; thus, there are a number of potential instrumental and calibration issues (e.g., labeling errors, calibrator position errors, delay tracking errors). These errors are detailed in I. Heywood et al. (2022), but at the time of these observations the dominant error was the delay tracking error; basically, the existing correlator model did not accurately transfer phases when switching between calibrator and target. In Section 4.1 we looked for systematic errors in the astrometry and attempted to correct for the bulk of these uncertainties. Our resulting offsets and rms deviations in source positions are comparable to similar values estimated for other data sets taken around the same time and using similar methods (I. Heywood et al. 2022; S. Goedhart et al. 2024; A. R. Taylor et al. 2024).

In order to improve S/N of the in-band spectral indices, we averaged different subbands together in six and three adjacent frequency bands (see Section 4). To test the reliability of this averaging method, we compared these derived spectral indices with those fitted using all 12 subbands. This is shown in Figure 4, where we compare the difference between the unaveraged subbands and the half-band averages (six adjacent frequencies) for 85,273 compact, single-component sources. The difference between these two spectral index values is within the best-fit errors for 73% of these compact, single-component sources, with the larger scatter occurring for low-S/N sources. In our search for known and candidate pulsars below we primarily used the  $\alpha$  values formed from the six subband averages. However, when we saw significant deviations between the other measures of  $\alpha$ , we visually inspected the unaveraged spectra. The differences were usually due to RFI or low S/N resulting in a poor fit from PyBDSF. In those few cases we simply manually refit the data, but there was an interesting subset of steep-spectrum sources that were too faint at higher frequencies that required a different search strategy (see Section 5.4). S. Goedhart et al. (2024) and W. D. Cotton et al. (2024) have detailed other issues related to the derivation of source spectral indices related to the lack of short spacings in these Galactic fields. This leads to a frequency-dependent "zero offset" error that can steepen  $\alpha$  from its true value. As this project is concerned with unresolved point sources, it should not be a serious problem unless the source is embedded in diffuse emission. Such cases can be identified by inspecting the images directly.

Interferometers like MeerKAT with orthogonal linearly polarized feeds have other instrumental effects. The most notable for polarimetric imaging is due to antenna pointing errors, which result in a frequency-dependent instrumental polarization signal also called "beam squint" (S. Sekhar et al. 2022). A. R. Taylor et al. (2024) have shown that the polarization leakage for MeerKAT is negligible (<0.2%) over most of the L-band frequency range but rises to several percent for frequencies above 1.4 GHz for sources whose position is offset more than 0.45 from the pointing center of the primary beam. For this particular project there is an added effect that reduces beam squint. We are looking for pulsars whose typically steep spectra ( $\alpha \simeq -1.7$ ) weight down the instrumental polarization by a factor of three at higher frequencies compared to the lower frequencies. Some bright, flat-spectrum sources with values of polarization of order 1%-2% could still be instrumental artifacts, but in any case their spectra would not make them promising pulsar candidates.

In Figure 5 we plot all 353 sources with detectable circular polarization as a function of Stokes I S/N. As we discussed above, we see a large number of detections at the 1% level that are likely instrumental artifacts arising from polarization leakage. For this reason bright Stokes I sources with |V/I| < 1% were eliminated from the sample. This value is in line with other estimates of polarization leakage from recent ASKAP and LOFAR polarimetric imaging surveys (Z. Wang et al. 2022b; J. R. Callingham et al. 2023). We will discuss the additional image artifacts (open circles) and the histogram in Section 5.2.

There is a positive skew in the distribution of V/I sources (Figure 5), which is most pronounced at low Stokes I S/N (<30) and high degrees of polarization (|V/I| > 30%). While certain coherent mechanisms favor amplification of the x-mode, which increases the degree of polarization (see M. Gudel 1992), we know of no physical mechanism that would favor the handedness of the polarization. The origin of this excess is also unlikely to be due to the data calibration and deconvolution process, since the numbers of positive and negative Stokes V sources are very similar in each of the mosaic fields.

We do not appear, however, to be overestimating the number of positive V/I sources. If this sample is dominated by false positives, we might expect the fraction of multiwavelength counterparts for positive V/I sources to drop compared to negative V/I sources at higher fractional polarization or lower S/N. As we note in Section 7.1, this appears not to be the case. Thus, we appear to be undercounting the number of real negative V/I sources. We have been unable to find a systematic error in our process that would undercount negative compact polarized radio sources. We followed a standard process to identify and then catalog the Stokes parameters for all significant sources in the mosaic images (Section 4) that is not biased against matching negative V Stokes with their Stokes I counterparts. Since we used a preliminary release of the MeerKAT images, it will be instructive to see whether this asymmetry persists in the final public data release (W. D. Cotton & SARAO Meerkat Bulge Survey Team 2024, in preparation).

### 5. Polarization Candidate Search

# 5.1. Known Pulsars

The efficacy of this survey for finding pulsar candidates can be tested using the sample of known pulsars. There are 81 known pulsars that lie within the survey area (see Figure 3 and Table 1). This is an undercount of the true number of pulsars.

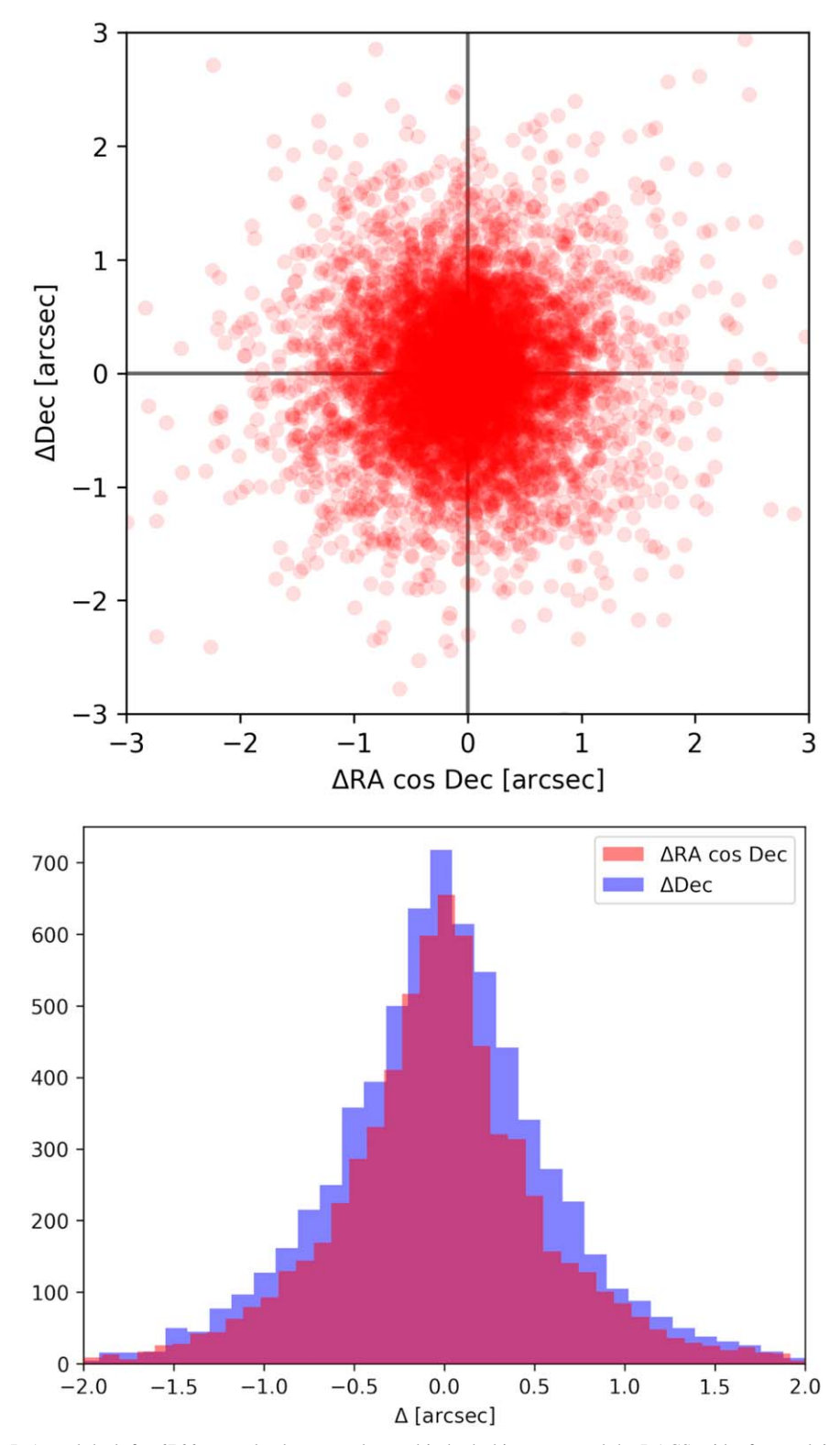


Figure 3. Angular offsets in R.A. and decl. for 6766 unresolved sources detected in both this survey and the RACS-mid, after applying astrometric corrections. See Section 4.1 for details.

There are two globular clusters (NGC 6522 and Terzan 5) that collectively have at least 45 pulsars. However, unless the pulsar is well separated from the cluster core, our images lack the angular resolution to resolve them individually (L. Zhang et al. 2020; R. Urquhart et al. 2020; F. Abbate et al. 2023). We identified three discrete, polarized point sources in these clusters for inclusion in Table 2. We suspect that the polarized

radio source identified as PSR J1748-2446ab may be an amalgamation of several overlapping pulsars.

For each mosaic pointing we first cross-matched our source catalog with the ATNF pulsar catalog <sup>15</sup> (R. N. Manchester

<sup>15</sup> http://www.atnf.csiro.au/research/pulsar/psrcat

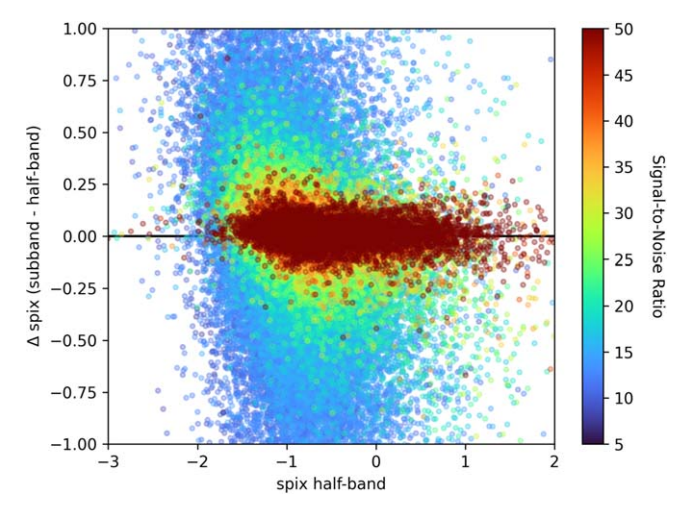


**Figure 4.** The difference in source spectral index derived using the two half-band-averaged images and the individual 12 subband images for 85,273 compact, single-component sources. Sources are colored according to their S/N in the full-band image.

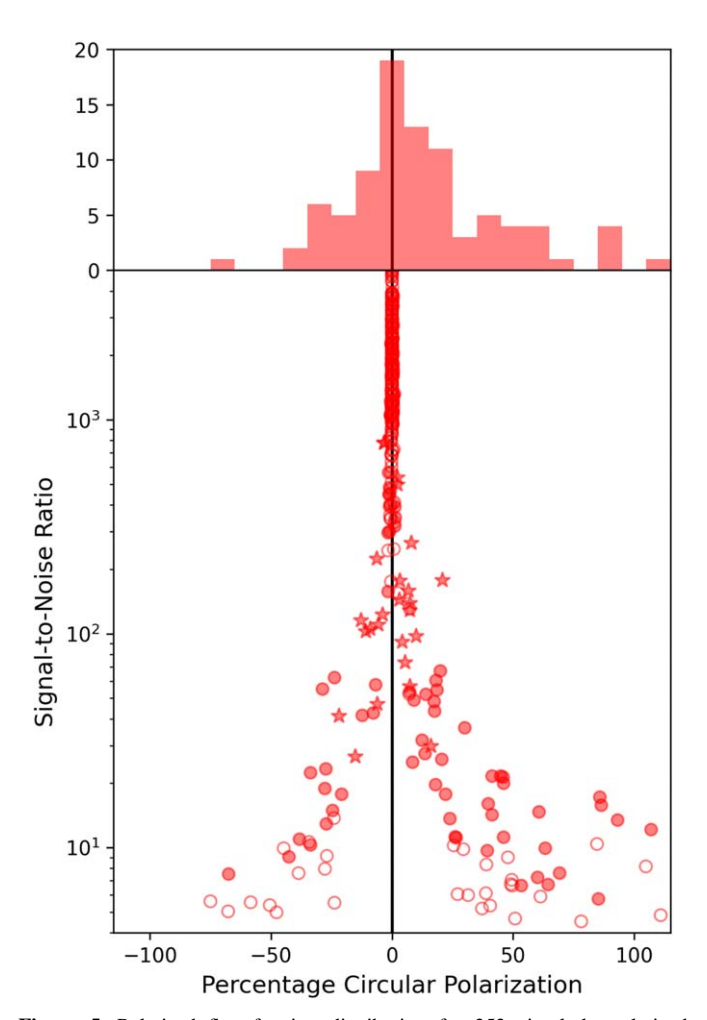


**Figure 5.** Polarized flux fraction distribution for 353 circularly polarized sources. Filled stars indicate known pulsars. Open circles are identified as image artifacts in Section 5.2 and not included in the upper histogram plot.

et al. 2005). When possible, we substituted ATNF catalog positions with newer values from the literature. For example, the identification of the rotating radio transient (RRAT) PSR J1739–2521 used a position from B. Y. Cui et al.

(2017). For Stokes *I*, this resulted in nearly a 100% detection rate. The quality of the pulsar position errors in this sample varies considerably, from subarcsecond accuracy for well-timed MSPs to arcminute positions for RRATs. As a result, and given our superb continuum sensitivity, it is likely that identifying pulsars relying on only Stokes *I* would result in a large number of detections of unrelated background extragalactic radio sources. To reduce these false positives, we required a positive pulsar match to also have either linear or circular polarization.

Table 2 lists the properties of the 39 known polarized pulsars detected in this survey. Circular polarization is listed under the column V/I, while linear polarization is listed under P/I; the S/N of each value is listed in the adjacent column. Our failure to correct our linear polarization images for a well-known noise bias (see Section 4) has a minor effect on the P/I values. We estimated its effect by propagating the errors by hand, including estimates for the noise bias, for a small number of pulsars in this table. We found that the estimates for the lower S/N values in the table were overestimated by 20%–40% in some cases. Nevertheless, we verified from visual inspection of the images that all of the detections of linear (and circular) polarization in Table 2 are real detections and not image artifacts.

In a number of cases the uncertainties on our measured positions (R.A./decl.), flux density (I), spectral indices ( $\alpha$ ), and polarization values are significant improvements over what is available in the literature. For the majority of the cases our positions are consistent with the known pulsar positions within joint measurement uncertainties, with a few exceptions. Specifically, the radio source identified with the MSP PSR J1653 -2054 is 4" from its timing position, while for PSR J1720-2446and PSR J1751-3323 the timing versus interferometric positions are offset by  $1.5\sigma$  and  $2\sigma$ , respectively. It is unlikely that these steep-spectrum, polarized point sources are false pulsar identifications, as such sources are rare. We show in the next section that the source density of circularly polarized sources is only  $0.5 \text{ deg}^{-2}$ , and F. de Gasperin et al. (2018) showed that <1% of radio sources have  $\alpha < -1.5$ . Proper motion might explain the offsets, but there are no published values in the literature. It seems likely that unmodeled timing residuals or optimistic position error estimates could account for the two normal pulsars, but the 4''offset for the MSP is difficult to explain.

The peak flux densities (I) of the pulsars in Table 2 range from about 0.4 to 40 mJy and are broadly consistent with the values in the ATNF catalog. The spectral indices  $\alpha$  range from +0.07 to -3.5, with a median value of  $-1.8 \pm 0.8$ , in reasonable agreement with the weighted mean spectral index of 441 pulsars of  $-1.60 \pm 0.03$  (F. Jankowski et al. 2018) and the more recent value of  $-1.78 \pm 0.6$  from 168 pulsars (A. Anumarlapudi et al. 2023). Nearly all of the pulsars have significant linear polarization, while less than 2/3 have significant circular polarization. The maximum linear polarization in Table 2 is 45%, while the maximum circular polarization is about half this amount. This range in polarization and the absolute values of the polarization percentages are consistent with the pulse-weighted averages from a large sample of pulsars (J. J. Rickard & W. M. Cronyn 1979; S. Johnston & M. Kerr 2018; A. Anumarlapudi et al. 2023). From the S. Johnston & M. Kerr (2018) sample of 600 pulsars, the mean linear polarization is 27% with a range from 1% to 100%, while the mean circular polarization is 8.4% with a range from 1% to 40%, with rare cases in excess of 60%. Moreover, there are 18 pulsars in Table 2 that are also

Table 2
The Polarization Properties of Known Pulsars

PSR Name	P	DM	R.A.	Decl.	I	α	V/I	S/N	P/I	S/N
	(ms)	$(pc cm^{-3})$	(h m s)	(°, ")	(mJy)		(%)		(%)	•
J1653-2054	4.1	56.5	16:53:30.79	-20:54:58.1	$2.19 \pm 0.01$	$-1.33 \pm 0.02$			1.7	6.2
J1719-2330	454.0	101.0	17:19:36.44	-23:30:07.3	$2.89 \pm 0.09$	$-1.16 \pm 0.44$			3.8	6.9
J1720-2446	874.3	104.3	17:20:22.57	-24:46:09.0	$0.45 \pm 0.02$	$-2.52 \pm 0.19$			14.1	7.1
B1717-29	620.4	42.6	17:20:34.11	-29:33:16.1	$2.68 \pm 0.01$	$-1.16 \pm 0.03$	-6.3	19.4	9.5	22.8
J1721-2457	3.5	48.2	17:21:05.50	-24:57:06.7	$1.37 \pm 0.01$	$-1.17 \pm 0.05$	-12.8	23.5	5.0	10.8
J1727-2739	1293.1	146.0	17:27:31.03	-27:38:53.0	$1.76 \pm 0.01$	$-1.50 \pm 0.04$	7.3	15.4	37.1	48.8
J1730-2304	8.1	9.6	17:30:21.69	-23:04:31.3	$4.36\pm0.02$	$-0.31 \pm 0.03$	20.9	86.4	21.6	120.6
B1730-22	871.7	41.1	17:33:26.41	-22:28:45.3	$12.97 \pm 0.09$	$-3.10 \pm 0.18$	3.1	12.5	12.6	61.9
J1734-2415	612.5	126.3	17:34:41.37	-24:16:15.0	$0.60 \pm 0.01$	$-1.45 \pm 0.10$			46.8	30.2
J1736-2457	2642.2	169.4	17:36:45.37	-24:58:02.4	$1.06 \pm 0.01$	$-2.14 \pm 0.05$		•••	24.3	19.4
B1736-29	322.9	138.6	17:39:34.28	-29:03:02.7	$4.86\pm0.04$	$-1.55 \pm 0.07$		•••	4.2	10.1
J1739-2521	1818.5	186.4	17:39:32.79	-25:21:09.3	$0.35\pm0.01$	$-2.54 \pm 0.16$			15.9	6.2
J1741-2733	893.0	147.4	17:41:01.33	-27:33:56.2	$1.89\pm0.02$	$-2.35\pm0.05$	-5.7	10.1	17.0	23.7
B1740-31	2414.7	193.1	17:43:36.72	-31:50:22.5	$2.09 \pm 0.02$	$-2.54 \pm 0.05$	4.2	8.2	13.7	32.4
J1743-3153	193.1	505.7	17:43:15.59	-31:53:05.8	$0.73 \pm 0.02$	$+0.07 \pm 0.15$	-22.0	14.0	23.1	17.7
J1744-3130	1066.1	192.9	17:44:05.71	-31:30:06.5	$0.74 \pm 0.02$	$-1.37 \pm 0.05$		•••	13.3	10.1
B1742-30	367.4	88.4	17:45:56.32	-30:40:22.9	$18.85\pm0.04$	$-1.87 \pm 0.10$	2.2	27.2	43.4	530.1
B1744-24A	11.6	242.1	17:48:02.26	-24:46:37.7	$3.45\pm0.04$	$-2.48 \pm 0.11$			4.0	6.0
J1748-2446ab	5.1	242.2	17:48:04.74	-24:46:41.8	$0.9 \pm 0.04$				19.0	7.2
J1748-3009	9.7	420.2	17:48:23.75	-30:09:11.6	$2.19 \pm 0.17$	$-2.25 \pm 0.38$	-7.1	6.8	16.6	19.8
B1746-30	609.9	509.4	17:49:13.51	-30:02:36.4	$4.84\pm0.05$	$-1.99 \pm 0.06$	-10.9	26.8	11.3	29.8
B1747-31	910.4	206.3	17:50:47.31	-31:57:44.5	$1.64 \pm 0.01$	$-1.58 \pm 0.03$	3.3	7.6	27.6	46.1
J1751-2857	3.9	42.8	17:51:32.65	-28:57:47.1	$0.85\pm0.07$	$-2.42 \pm 0.75$			37.0	14.6
J1751-3323	548.2	296.7	17:51:32.76	-33:23:34.5	$1.59 \pm 0.01$	$-0.59 \pm 0.03$	•••	•••	15.4	40.2
B1749-28	562.6	50.4	17:52:58.67	-28:06:38.3	$39.22\pm0.05$	$-3.01 \pm 0.01$	-3.2	73.9	11.2	267.7
J1754-3443	361.7	188.7	17:54:37.34	-34:43:55.0	$1.01\pm0.03$	$-1.63 \pm 0.59$	16.2	6.2	10.3	5.6
J1759-2922	574.4	79.4	17:59:48.26	-29:22:08.1	$0.83 \pm 0.01$	$-2.61 \pm 0.07$	5.5	5.3	19.9	21.7
J1759-3107	1079.0	128.3	17:59:22.05	-31:07:22.0	$1.31\pm0.01$	$-1.49 \pm 0.04$	-3.9	6.7	16.8	27.1
B1758-29	1081.9	125.6	18:01:46.82	-29:20:39.6	$2.95\pm0.01$	$-1.79 \pm 0.02$	8.0	31.6	43.5	170.4
J1801-3210	7.5	177.7	18:01:25.90	-32:10:53.8	$0.67 \pm 0.01$	$-2.15 \pm 0.10$	•••	• • • •	13.0	13.7
B1800-27	334.4	165.5	18:03:31.70	-27:12:05.2	$1.41\pm0.02$	$-1.27 \pm 0.09$	7.5	8.4	33.4	46.7
J1803-3002A	7.1	192.6	18:03:35.11	-30:02:00.8	$0.66\pm0.01$	$-2.15 \pm 0.09$	-6.9	5.8	•••	•••
J1803-3329	633.4	170.9	18:03:44.45	-33:29:10.9	$0.92\pm0.01$	$-1.26\pm0.05$	-9.1	13.9	8.3	13.4
J1804-2717	9.3	24.7	18:04:21.15	-27:17:32.2	$0.69 \pm 0.03$	$-3.50 \pm 0.18$	-15.2	8.4	39.7	28.0
J1804-2858	1.5	232.5	18:04:01.53	-28:58:47.2	$1.09\pm0.01$	$-2.45 \pm 0.05$	9.9	15.5	5.4	8.6
B1804-27	827.8	313.0	18:07:08.50	-27:15:03.7	$1.54\pm0.03$	$-3.19\pm0.22$	-6.1	5.0	•••	•••
J1808-3249	364.9	147.3	18:08:04.51	-32:49:32.9	$1.65\pm0.01$	$-1.10\pm0.03$	6.8	16.6	8.8	21.5
J1812-2748	237.0	104.0	18:12:40.59	-27:48:04.5	$0.41\pm0.04$	$-0.42 \pm 1.40$	•••	•••	25.8	5.9
J1812-3039	587.5	141.4	18:12:44.90	-30:39:22.2	$0.46\pm0.01$	$-2.19\pm0.12$	•••	•••	28.1	18.7

**Note.** The positions (R.A./decl.), flux densities (I), spectral indices ( $\alpha$ ), and polarization fraction V/I and P/I come from this work, while the period (P) and dispersion measure (DM) are taken from the ATNF Pulsar Catalog (R. N. Manchester et al. 2005).

found in common with S. Johnston & M. Kerr (2018). We detect linear and/or circular polarization of the right magnitude from all but their two faintest pulsars. The direction of polarization is reversed in these two samples, suggesting different conventions between MeerKAT polarization and the known pulsar sample.

Summarizing, we find polarized point sources coincident with approximately 50% of the known pulsars, and their properties (flux density, spectral index, and polarization) are consistent with these radio sources as known pulsars.

### 5.2. Circularly Polarized Sources

For each mosaic field we carried out a search for circular polarized sources. We started by identifying single Gaussian component circularly polarized sources within the catalog made from each mosaic with  $|V/I| \geqslant 1\%$ . The source density of circularly polarized sources is only  $0.5~{\rm deg}^{-2}$ , so this approach was sufficient to identify all the radio sources with nonzero Stokes V and sort them in order of decreasing fractional polarization.

To complete the search, these remaining sources were visually inspected directly from the Stokes I and V images to look for suspect signals (see Section 4.2). The most common V Stokes artifacts were produced from sidelobe contamination from bright radio sources, while a smaller number were flagged as suspicious, as they were found at the far edge of the antenna's field of view, or the Stokes V signal was offset from the Stokes I peak by a significant fraction of the synthesized beam. Of the 100 initial sources from the catalog search, 38 were flagged as suspicious or image artifacts, another was a duplicate identification from two adjacent mosaics, and another was a known pulsar that was found owing to an improved timing position (L. Zhang et al. 2020). The V/I values for the artifacts (open circles) and for both the known pulsars (filled stars) and our sources (filled circles) are shown in Figure 5. While the V/I values for the known pulsars in Table 2 are evenly distributed, the sources in Table 3 are skewed toward more positive V/I values. As we discuss in Section 4.2, the

**Table 3**Circularly Polarized Sources

R.A.	Decl.	l	b	I	α	V/I	S/N	Notes
(h m s)	(° ', ")	(deg)	(deg)	(mJy)		(%)	~/	- 10000
16:45:59.27	-18:22:20.1	0.96	17.21	$0.39 \pm 0.01$	$0.53 \pm 0.3$	13.5	7.0	O, IR; YSO
16:56:48.02	-23:09:01.8	358.6	12.31	$0.81 \pm 0.02$	$0.21 \pm 0.16$	-7.9	5.2	O, IR; A05 star
17:00:27.74	-22:07:42.7	359.96	12.24	$0.08 \pm 0.01$	$-1.07 \pm 0.70$	-67.6	8.0	O, IR; late M dwarf
17:11:23.02	-24:38:49.6	359.37	8.74	$0.16\pm0.02$	$-0.64 \pm 0.64$	-42.8	9.6	O, IR: YSO
17:12:08.72	-23:09:49.8	0.7	9.45	$0.26\pm0.01$	$0.16\pm0.31$	20.4	7.8	O, IR: YSO
17:13:34.15	-24:10:44.5	0.05	8.6	$3.88 \pm 0.01$	$0.07 \pm 0.03$	-1.1	5.6	
17:16:29.81	-26:55:16.7	358.16	6.49	$0.19 \pm 0.01$	$0.43 \pm 0.96$	60.6	12.5	X, O, IR: YSO
17:17:41.97	-28:56:19.4	356.65	5.11	$0.08 \pm 0.01$	$-1.12 \pm 0.96$	64.4	6.3	X, O, IR: YSO
17:19:56.71	-24:57:04.2	0.24	6.97	$0.32\pm0.01$	$1.12\pm0.4$	-27.4	11.1	O, IR: YSO
17:20:18.40	-26:52:07.8	358.69	5.82	$0.20\pm0.01$	$-1.87\pm0.31$	-27.8	7.9	•••
17:20:55.04	-27:20:41.5	358.38	5.44	$0.27\pm0.01$	$0.15\pm0.31$	-33.8	12.6	X, O, IR: binary star
17:23:29.79	-28:20:36.1	357.87	4.4	$0.59 \pm 0.01$	$-1.52 \pm 0.11$	-12.5	6.2	•••
17:24:16.36	-27:30:43.8	358.66	4.73	$0.53 \pm 0.01$	$0.88 \pm 0.17$	17.3	11.7	X, O, IR: YSO
17:27:28.51	-25:28:20.6	0.76	5.26	$0.57 \pm 0.01$	$0.51 \pm 0.13$	13.9	10.0	O, IR: YSO
17:27:52.07	-27:27:24.6	359.15	4.09	$0.18 \pm 0.02$	$-1.99 \pm 0.45$	26.4	6.2	•••
17:28:20.26	-26:08:16.6	0.31	4.73	$0.22 \pm 0.01$	$-2.9 \pm 0.26$	17.8	5.5	
17:29:31.96	-27:31:37.8	359.29	3.75	$0.11 \pm 0.02$	$-1.05 \pm 0.67$	60.1	7.8	
17:32:50.03	-23:54:14.4	2.75	5.1	$5.31 \pm 0.01$	$-1.16 \pm 0.01$	-1.4	9.8	
17:37:57.25	-27:33:05.3	0.29	2.16	$3.74 \pm 0.01$	$-0.13 \pm 0.02$	-1.7	7.0	
17:40:06.78	-28:05:33.9	0.08	1.47	$0.86 \pm 0.02$	$-1.46 \pm 0.15$	30.0	22.2	•••
17:44:08.71	-24:24:53.4	3.69	2.64	$1.19 \pm 0.02$	$-2.20 \pm 0.09$	19.9	18.8	•••
17:45:43.03	-26:58:53.9	1.68	1.0	$3.34\pm0.02$	$-0.57 \pm 0.04$	-1.8	5.1	X
17:47:18.05	-33:09:17.4	356.58	-2.5	$0.91 \pm 0.01$	$-1.99 \pm 0.08$	-23.9	24.4	•••
17:51:06.84	-32:18:28.5	357.72	-2.75	$0.58 \pm 0.01$	$0.92 \pm 0.15$	18.4	14.6	X, O, IR: YSO
17:51:15.97	-29:43:52.0	359.95	-1.46	$0.8 \pm 0.03$	$-1.74 \pm 0.22$	8.3	5.6	•••
17:52:29.06	-28:49:05.6	0.87	-1.23	$1.07 \pm 0.02$	$-0.86 \pm 0.12$	9.0	7.1	•••
17:53:06.42	-29:30:00.8	0.36	-1.69	$0.26 \pm 0.02$	$-1.51 \pm 0.51$	26.0	6.5	•••
17:53:06.50	-28:51:26.2	0.91	-1.37	$0.22\pm0.02$	$-0.84 \pm 0.53$	46.0	8.4	G: PSR?
17:53:39.01	-33:31:28.4	356.94	-3.83	$0.15 \pm 0.01$	$-1.17 \pm 0.38$	23.7	5.4	•••
17:55:24.86	-33:58:30.7	356.73	-4.37	$0.16 \pm 0.01$	$-0.28 \pm 0.37$	39.5	9.0	O, IR
17:59:20.04	-28:29:56.6	1.91	-2.37	$0.13 \pm 0.01$	$-2.24 \pm 0.57$	-33.7	5.3	
17:59:20.59	-30:15:48.7	0.37	-3.24	$0.17 \pm 0.01$	$1.66 \pm 0.58$	22.1	5.2	O, IR: $\beta$ Cep.
18:00:12.33	-27:44:32.5	2.66	-2.16	$0.12 \pm 0.02$	$0.25 \pm 1.63$	69.1	8.3	crowded field
18:00:32.14	-27:35:36.0	2.83	-2.15	$0.29 \pm 0.02$	$-2.93 \pm 0.28$	-20.9	6.2	
18:04:03.38	-33:31:53.0	358.01	-5.72	$3.73 \pm 0.01$	$0.26 \pm 0.02$	-1.0	5.9	X
18:05:26.44	-29:29:54.6	1.69	-4.02	$0.18 \pm 0.01$	$-4.31 \pm 0.38$	86.3	21.5	X, O, IR: K star
18:06:31.55	-29:21:37.0	1.93	-4.16	$0.06 \pm 0.01$	$0.27 \pm 0.99$	85.2	7.0	•••
18:11:37.21	-32:06:50.9	0.02	-6.44	$0.36 \pm 0.01$	$-0.49 \pm 0.13$	17.4	9.3	
18:13:45.72	-33:17:38.6	359.18	-7.39	$0.18 \pm 0.01$	$-1.71 \pm 0.45$ $-0.7 \pm 0.02$	106.8	24.8	O; M dwarf
18:15:21.88	-32:53:02.1	359.71	-7.49	$3.17 \pm 0.01$		1.3	5.9	•••
18:16:34.34 18:17:09.82	-32:34:12.4 -33:17:31.2	0.11 359.52	-7.57 $-8.02$	$0.45 \pm 0.01$	$-1.06 \pm 0.11$ $0.62 \pm 0.48$	7.2 $-24.6$	5.1 5.5	 O ID. VCO
18:17:09.82				$0.13 \pm 0.01$				O, IR: YSO
18:19:52.24	-32:54:18.2 $-29:16:34.4$	360.0 3.38	-8.09 $-6.68$	$0.2 \pm 0.01$ $0.27 \pm 0.02$	$-1.18 \pm 0.25$ $0.68 \pm 0.63$	45.7 -27.2	14.2 5.1	O, IR: binary star
18:29:52.06	-29.10.34.4 -33:55:40.8	0.13	-0.08 -10.67	$0.27 \pm 0.02$ $0.2 \pm 0.01$	$0.08 \pm 0.03$ $1.2 \pm 0.4$	41.2	12.2	O, IR: YSO
			-10.67 $-10.58$		$0.61 \pm 0.37$			
18:29:52.97 18:34:49.11	-33:43:04.7	0.33		$0.16 \pm 0.01$ $5.4 \pm 0.01$	$-0.5 \pm 0.02$	46.0	11.0	O, IR: star
18:35:01.56	-35:05:25.8 $-34:18:20.1$	359.51 0.25	-12.09 $-11.79$	$3.18 \pm 0.01$	$-0.3 \pm 0.02$ $0.33 \pm 0.02$	-1.2 1.1	9.6 5.1	
	-36:07:49.2	359.14						
18:41:54.78			-13.83	$0.14 \pm 0.01$	$-1.58 \pm 0.55$	-38.4	8.5	O, IR: YSO
18:43:58.38 18:50:19.66	-35:59:10.0 -36:29:12.8	359.45 359.49	-14.15 $-15.53$	$0.28 \pm 0.01$ $3.97 \pm 0.01$	$1.31 \pm 0.27$ $-0.14 \pm 0.01$	12.3 1.0	5.7 6.5	O, IK: 150
18:52:26.04	-36:29:12.8 -37:30:37.8	359.49 358.67	-15.55 -16.3	$0.21 \pm 0.01$	$-0.14 \pm 0.01$ $-2.70 \pm 0.37$	41.2	9.5	X, O, IR: M4.5 dwarf
18:57:45.15	-37:19:38.3	359.25	-10.3 $-17.22$	$0.21 \pm 0.01$ $0.53 \pm 0.01$	$-2.70 \pm 0.37$ $-0.05 \pm 0.12$	-28.7	9.3 22.7	X, O, IR: W4.5 dwarf
19:00:51.24	-36:13:15.8	339.23 0.57	-17.22 $-17.39$	$0.33 \pm 0.01$ $0.06 \pm 0.01$	$-0.03 \pm 0.12$ $-0.63 \pm 0.69$	-28.7 53.4		IR: YSO
19:00:51.24 19:01:40.56	-36:13:15.8 -36:44:32.4	0.57	-17.39 -17.74	$0.06 \pm 0.01$ $0.08 \pm 0.01$	$-0.63 \pm 0.69$ $2.08 \pm 0.76$	63.3	5.2 9.4	O, IR: YSO
19:01:48.04 19:01:55.64	-36:57:20.5 -37:39:41.1	359.92 359.24	-17.84 $-18.11$	$0.61 \pm 0.01$ $5.34 \pm 0.01$	$0.56 \pm 0.12$ $0.75 \pm 0.01$	$18.0 \\ -1.5$	18.7 13.0	IR: YSO X, O, IR: YSO
19:01:55.64	-37:39:41.1 -37:16:41.7	359.24 359.7	-18.11 $-18.19$	$0.16 \pm 0.01$	$-0.55 \pm 0.01$ $-0.55 \pm 0.28$	-1.5 44.8	13.0	O, IR: YSO
19:05:06.55	-37:10:41.7 -37:03:49.5	0.16	-18.19 $-18.74$	$0.10 \pm 0.01$ $0.19 \pm 0.01$	$-0.33 \pm 0.28$ $-0.18 \pm 0.32$	85.6	24.7	O, IK: 150 
19:07:38.78	-37:08:55.9	0.16	-16.74 $-19.0$	$6.64 \pm 0.01$	$-0.18 \pm 0.32$ $-1.08 \pm 0.01$	-1.1	7.7	
17.07.38.78	-51.08.33.9	0.10	-19.0	$0.04 \pm 0.01$	$-1.00 \pm 0.01$	-1.1	1.1	•••

Note. O = optical counterpart; IR = infrared counterpart; X = X-ray counterpart; G = gamma-ray counterpart. YSO = young stellar object. Details on individual source detections are given in Section 6.

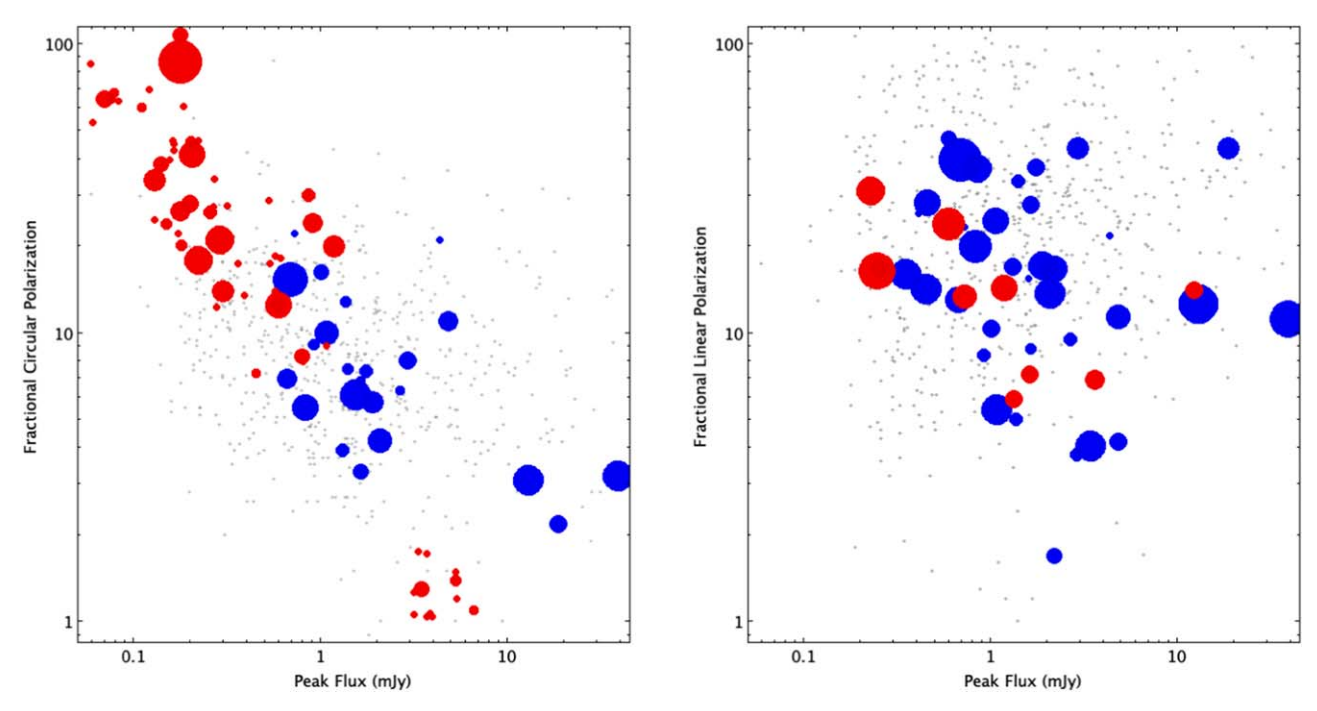


**Figure 6.** Polarized sources (red) and known pulsars (blue). The left panel plots the absolute value of the circular polarization fraction vs. Stokes *I* flux density, while the right panel plots the linear polarization vs. Stokes *I* flux density. The size of the circle for each point is proportional to the spectral index, with larger circles indicating steeper negative spectral indices. Gray points are polarization and flux density values taken from the compilation of S. Johnston & M. Kerr (2018).

positive V/I excess occurs at lower values of Stokes I S/N. The known pulsars are on average brighter than our remaining circular polarized sources and thus do not show this skew.

The "V" entries in the sixth column of Table 1 list the number of circularly polarized sources found in each of the mosaic pointings. Our final sample of 60 circularly polarized sources is given in Table 3 and is plotted in Figure 6 (left). While the number of known pulsars in Figure 3 increases with decreasing Galactic latitude as expected, the distribution of circular polarized sources in Table 1 is more uniform, with clusters of sources at high latitude (e.g., G000.0-17.5). This is suggestive that not all of these circularly polarized sources are pulsars, but rather are from some other source population(s). This hypothesis is further supported by the source distribution in Figure 6. The mean spectral index of our 60 sources is -0.6, versus -1.8 for the known pulsars in Table 2. Likewise, the fractional polarization for the known pulsars in these fields ranges from 2% to 20%, while our sources are distributed over a much larger range.

The absence of sources in the lower left corner of the panels of Figure 6 is due to a noise bias, the result of cutting off low-S/N detections (see also J. Pritchard et al. 2021; C. Sobey et al. 2022; Z. Wang et al. 2022b; J. R. Callingham et al. 2023). The fixed MeerKAT integrations introduce a strong bias in our polarization measurements. For example, our sources must have a peak Stokes I flux in excess of  $\sim 1$  mJy to have a measured V/I < 5%. As this is rather bright, we expect that most such pulsars will have been found by previous time-domain surveys, while our sources on average will be fainter than that. The real distribution of pulsar circular polarization with peak flux is more closely approximated by the large sample of S. Johnston & M. Kerr (2018) plotted in Figure 6 as light-gray points. In that sample, there is no noise bias because the integration times for each of the pulsars are determined in

order to achieve an S/N sufficient to measure their polarization properties.

The lack of bright, highly polarized sources, however, is real (i.e., upper right corner). As we noted in Section 4.2, the cluster of bright (>3 mJy), weakly polarized (1%–2%) sources in the lower right corner could still have some false positives among them. While there are some steep-spectrum sources in this low-polarization sample that may have been missed by previous pulsation searches, we suspect that most are extragalactic sources with weak circular polarization or beam squint artifacts. There is support for this hypothesis since the median spectral index of this small sample more closely resembles that of extragalactic sources than pulsars (F. de Gasperin et al. 2018). In Section 6 we will use multiwavelength counterparts in an effort to distinguish promising pulsar candidates from other source populations.

### 5.3. Linearly Polarized Sources

A different approach was needed for identifying linearly polarized pulsar candidates. The Stokes Q and U mosaic images have rich structure, likely due to Faraday rotation from the interstellar medium of large-scale Galactic emission. Moreover, the areal density of linearly polarized sources in the master catalog is large, approximately  $40 \, \mathrm{deg}^{-2}$ , with the majority of the polarized emission coming from extended sources (active galactic nucleus jets, supernova remnants, etc.). More stringent selection criteria were needed to achieve a manageable number of polarized sources. For each mosaic pointing we first eliminated extended sources by requiring that the compactness criterion exceed 0.9 and that the source not be fit by multiple Gaussian components (see Section 4).

Once we identified a sample of compact radio sources, we further required that the spectral index  $\alpha \lesssim -1.5$  and the fractional linear polarization |P/I| > 5%. These criteria restrict the phase space to pulsar-like properties in order to keep the

**Table 4**Linearly Polarized Sources

R.A. (h m s)	Decl. (° ', ")	l (deg)	b (deg)	I (mJy)	α	P/I (%)	S/N
17:01:54.67	-22:50:08.3	359.58	11.55	$0.73 \pm 0.01$	$-2.00 \pm 0.09$	13.3	11.6
17:18:37.15	-23:35:10.5	1.21	7.99	$1.62 \pm 0.02$	$-1.52 \pm 0.11$	7.2	10.4
17:26:26.80	-30:48:09.2	356.19	2.5	$3.63 \pm 0.03$	$-1.65 \pm 0.08$	6.9	14.9
17:31:21.50	-25:02:35.7	1.6	4.76	$12.33 \pm 0.02$	$-1.48 \pm 0.01$	14.0	197.0
17:44:08.71	-24:24:53.4	3.69	2.64	$1.19 \pm 0.02$	$-2.20 \pm 0.09$	14.3	12.8
18:18:22.84	-32:44:16.0	0.13	-7.99	$0.23 \pm 0.01$	$-2.34 \pm 0.26$	31.0	12.1
18:21:46.77	-32:47:27.8	0.41	-8.65	$0.26 \pm 0.01$	$-1.48 \pm 0.33$	16.6	7.3
18:24:17.96	-32:38:05.4	0.79	-9.05	$0.60 \pm 0.06$	$-2.66 \pm 0.54$	23.7	13.6
18:27:31.72	-32:52:38.9	0.88	-9.77	$1.33 \pm 0.02$	$-1.51 \pm 0.08$	5.9	12.3
18:37:36.28	-33:50:13.8	0.92	-12.08	$0.25\pm0.01$	$-3.04 \pm 0.29$	16.3	7.4

Table 5
Low-band Circularly Polarized Sources

R.A. (h m s)	Decl. (° ', ")	l (deg)	b (deg)	<i>I</i> (mJy)	$\alpha$	V/I (%)	S/N
17:27:34.51	-26:09:57.1	0.19	4.86	$0.07 \pm 0.01$	$-1.87 \pm 0.72$	64.0	5.5
17:31:14.95	-27:35:32.4	359.45	3.39	$0.30 \pm 0.01$	$-2.18 \pm 0.22$	13.9	5.3
18:02:21.53	-32:54:38.0	358.38	-5.10	$3.46 \pm 0.01$	$-1.61 \pm 0.01$	1.3	5.5
18:24:17.96	-32:38:05.4	0.79	-9.05	$0.60 \pm 0.06$	$-2.66 \pm 0.54$	12.4	6.2
18:51:20.86	-35:46:19.5	0.26	-15.44	$0.18 \pm 0.01$	$-1.36\pm0.29$	20.0	5.3

false positives to a manageable level, but they also introduce a selection bias into the sample. Approximately 50% of all known pulsars have spectral indices steeper than -1.5(F. Jankowski et al. 2018), and 95% of pulsars have linear polarization above 5% (S. Johnston & M. Kerr 2018). Despite these more restrictive criteria, visual inspection of the polarization images resulted in about 80% of the detections being identified as either image artifacts or extragalactic. The largest false positives were extragalactic sources, seen as compact polarized knots in jets, double radio sources, and clusters of radio sources. Our final sample of 10 linearly polarized sources is given in Table 4 and is plotted in Figure 6. The "P" entries in the sixth column of Table 1 list the number of linearly polarized sources found in each of the mosaic pointings, including two sources identified in more than one mosaic field.

The properties of these linearly polarized sources are listed in Table 4 and plotted in Figure 6 (right). Not surprisingly, given our selection criteria, the spectral index distribution and high fractional polarization are similar to the known pulsars in Table 2 and the larger sample of linear polarization measurements from S. Johnston & M. Kerr (2018). There are some compelling pulsar candidates in Table 4 based on the compactness, steep-spectrum, and polarization criteria. J173121.50-250235.7 is an exceptionally bright steep-spectrum source with a Stokes I flux density of 12 mJy and is 16% polarized, while J174408.71-242453.4 is also bright (I = 1.2 mJy) and has a steep spectrum but has both significant linear and circular polarization. It is likely, however, that these sources are relatively nearby and not in the bulge. Given our central observing frequency ( $\nu = 1284 \, \text{MHz}$ ) and the bandwidth of the 12 subband averages ( $\delta \nu \simeq 50 \, \text{MHz}$ ) that we used (Section 2), we expect significant Faraday bandwidth depolarization for rotation measures (RMs) in excess of  $235 \text{ rad m}^{-2}$  (see Equation (1) of S. D. Hyman et al. 2021), well below RM values reported near the GC (J. D. Livingston et al. 2021).

Our main conclusion from this pilot effort is that linearly polarized images are a suboptimal method for identifying pulsar candidates. While we are confident that the detections in Table 4 are real linearly polarized sources in the images, the overwhelming number of artifacts and other real source populations required additional selection criteria that introduce significant selection biases, making the method ill-suited for surveys of the bulge or elsewhere in the Galaxy.

#### 5.4. Low-band Circularly Polarized Sources

There are significant numbers of sources in the catalog that are not detected with  $5\sigma$  significance across the full frequency range of the MeerKAT L-band receivers. This may be the result of channel flagging due to RFI, or due to the fact that the source has a sufficiently steep spectrum that it falls below the noise threshold at higher frequencies. As we are looking for steep-spectrum pulsars, we considered additional sources that met our selection criteria using only the lower half of the band centered at 1.022 GHz. We might expect that the majority of such sources will be weak and have a steep spectrum in order for them to have been missed by the selection criteria in Sections 5.2 and 5.3.

Using only the low-frequency end of the L band, we found a total of nine compact, circularly polarized (|V/I| > 1%) sources and 32 linearly polarized (P/I > 5%) sources. None of the low-band linearly polarized sources passed our visual inspection. Of the nine low-band circularly polarized sources, three were image artifacts and one was a known pulsar, PSR J1748-3009 (Table 2). The final list of five sources is shown in Table 5. The full-band peak flux density is listed, whereas the percent polarization and S/N are derived from the low end of the band. We note that one of these sources, J182417.96-323805.4, is also detected as a linearly polarized source in Table 4.

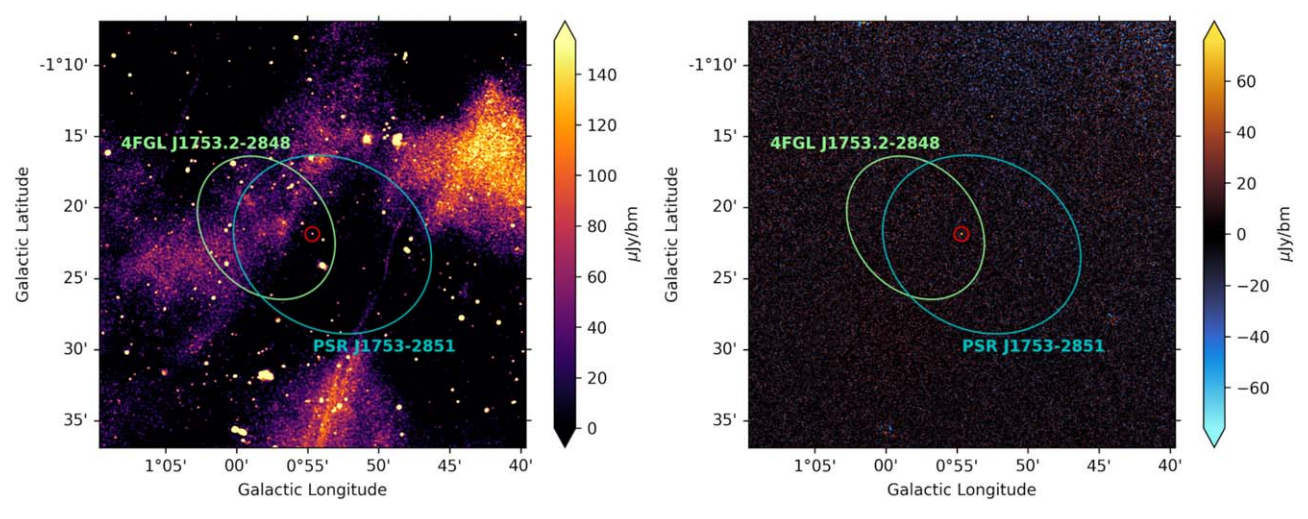


**Figure 7.** Stokes *I* (left) and Stokes *V* (right) cutout images centered on our circularly polarized source J175306.50–285126.2 (red circle). We show the error circles for the Fermi source 4FGL J1753.2–2848 and the known pulsar PSR J1753–28. A possible association is suggested but not proven between our polarized radio source, the known pulsar, and the gamma-ray source.

### 6. Additional Selection Criteria

As previously noted in Section 5.2, there are other source populations among the circularly polarized sources in Table 3 that are not pulsars. This is less likely for the linearly polarized sources in Table 4 since we have used more stringent pulsarlike criteria to limit the false positives. Extragalactic radio sources are not expected to be a significant contaminant for circular polarization. Apart from fast radio bursts, which we do not expect to detect, the circular polarization from extragalactic radio sources rarely exceeds 1% (J.-P. Macquart 2002). On the other hand, magnetically active single and binary stars can produce nonthermal (coherent and incoherent) radio emission that can be strongly polarized. A comprehensive list of the types of radio stars expected and the origin of their polarized emission can be found in J. Pritchard et al. (2021) and J. R. Callingham et al. (2023) for centimeter and decimeter wavelengths, respectively.

A multiwavelength approach can be useful both for identifying these stellar populations and for bolstering pulsar candidates. To this end, in the next several subsections we search for counterparts to our polarized radio sources at gamma-ray, X-ray, optical, and infrared wavelengths. Where possible, we also include archival radio data to better constrain the in-band spectral indices and to search for variability. However, before focusing on any wavelength-specific searches, we began by searching a 2' radius around each of the sources in Tables 3–5 using the SIMBAD database (M. Wenger et al. 2000). There are two immediate findings from this search that help to inform the multiwavelength searches below. The first is that, given our astrometry accuracy (Section 4.1), the high stellar densities in the bulge will likely result in significant false positives in the optical/near-IR. We discuss our efforts to mitigate this in Section 6.2. The second finding is that there are a large number of unexpectedly bright, nearby stars or young stellar objects (YSOs) within 5" of our circularly polarized sources. For example, one of our strongly polarized sources (V/I = 86%), J190625.66-370349.5, lies close to the highproper-motion, naked-eye star  $\gamma$  CrA with G = 4.8 mag. Proper-motion corrections will be needed to assess whether these are real associations (see Section 6.2), but the preponderance of SIMBAD matches of stars with G-band

magnitudes in excess of 10–15 mag is suggestive, given their rarity among the known Gaia stellar brightness distribution (Gaia Collaboration et al. 2021).

### 6.1. High-energy Counterpart Searches

The Fermi Gamma-ray Space Telescope has discovered pulsed emission from nearly 300 pulsars (D. A. Smith et al. 2023), but there remain many more candidates with distinct spectral and temporal signatures among the unknown or unassociated gamma-ray sources (S. Abdollahi et al. 2022). We searched for matches between our polarized pulsar sources and the 2577 unknown or unassociated Fermi gamma-ray sources in the latest 14 yr Fermi-LAT incremental catalog (J. Ballet et al. 2023). We find one match of 4FGL J1753.2 -2848 with the circularly polarized source J175306.50 -285126.2 (|V/I| = 46%) in Table 3. The unknown Fermi source is associated with the X-ray source 1RXS J175328.7 -285014, and its best-fit energy spectrum is compatible with pulsar spectral characteristics (D. A. Smith et al. 2023). We note that the 86 ms period PSR J1753-28 lies 94" from this polarized radio source, but the pulsar position is poorly constrained ( $\pm 7'$ ; A. D. Cameron et al. 2020), preventing us from making a positive identification (see Figure 7). An improved timing position for PSR J1753-28 and a measurement of its period derivative and spin-down energy could test whether this polarized radio source is the pulsar and whether it is capable of powering the gamma-ray emission. None of the sources in Tables 4 and 5 have Fermi counterparts.

Young radio pulsars and MSPs show a scaling of their spin-down energy (È) with X-ray flux (e.g., A. Possenti et al. 2002). To this end we searched for X-ray counterparts of our polarized radio sources (Tables 3–5) in the Chandra and SWIFT bulge surveys (P. G. Jonker et al. 2011, 2014; A. Bahramian et al. 2021). No matches were found at the lower Galactic latitudes where these X-rays surveys were carried out. There was more success using the Chandra Source Catalog 2.0 (I. N. Evans et al. 2010) and the recently released 6-month sky survey with the eROSITA telescope array in the 0.2–2.3 keV energy range (A. Merloni et al. 2024). In the Chandra catalog we found two point sources within 4" of the circularly polarized sources in Table 3. In the eRosita catalog we found eight X-ray sources

that lie within the joint radio/X-ray position uncertainties, despite the fact that this initial data release covers only half of our bulge survey area (i.e., all Galactic latitudes for longitudes west of Sgr A\*). There were no X-ray counterparts to any of the polarized sources in Tables 4 and 5.

Most of the radio spectra of these X-ray sources are flat or inverted (i.e.,  $\alpha \gtrsim -0.6$ ), with one exception. J180526.44 -292954.6 has  $\alpha = -4.31$  and appears to be associated with 2CXO J180526.4-292952. We discuss this and other sources in more detail in Section 6.2, and we show that the majority of the X-ray associations likely originate from active stars and YSOs. All of these gamma-ray and X-ray matches are identified in the Table 3 as G and X, respectively.

### 6.2. Optical and Infrared Counterparts

Our search for optical and infrared counterparts of the polarized sources (Tables 3–5) used the latest Gaia data release (Gaia Collaboration et al. 2023) and the ALLWISE catalog from the Wide-field Infrared Survey Explorer (WISE; E. L. Wright et al. 2010). Astropy code was written in order to make proper-motion corrections of the Gaia stars to the mean epoch of the MeerKAT observations (2020.3) for all radio sources in Tables 3–5.

Most isolated pulsars do not have detectable O/IR emission (J. Antoniadis 2021). Thus, the detection of optical/IR emission at centimeter wavelengths generally means that the circularly polarized source is a star, e.g., magnetically active dwarfs, YSOs, and interacting binaries (J. Pritchard et al. 2021). However, caution is warranted since our main goal is identifying MSP candidates in the bulge and they can have a faint optical/IR companion. In the compilation of K. I. I. Koljonen & M. Linares (2023) the majority of known compact MSP binaries have *G*-band magnitude companions fainter than 18th mag, but there are a small number of systems in the 14–18 mag range. When possible, we use other criteria (e.g., colors) in looking at matches in this magnitude range.

T. J. Wilson & T. Naylor (2018) point out two additional challenges. The first problem is false identifications arising as a result of the high star density and extreme crowding in the bulge. For each possible association of a star of magnitude G (or W1 for WISE) we estimate the probability of chance coincidence by using the number density of stars above this magnitude within a 1' radius of the radio source. We flag as suspect any associations with probabilities above 0.5%. In practice, given our astrometric error, this resulted in a magnitude cutoff of about G > 15.6 mag for Gaia sources. As a final check, we visually inspect available optical and WISE images of each field to identify directions with extreme crowding. A second issue raised by T. J. Wilson & T. Naylor (2018) is the nonidentification of the brightest sources (G < 10 or W 1 < 8 mag). This is in part due to position errors caused by the saturation of the detectors and small systematic effects in the proper motion of stars (T. Cantat-Gaudin & T. D. Brandt 2021).

None of the 10 (steep-spectrum) linearly polarized sources in Table 4 had IR counterparts or Gaia proper-motion-corrected matches within the uncertainty of our radio positions. A similar null result was obtained for the sources in Table 5.

The source matching of the ALLWISE catalog with our circularly polarized sources in Table 3 gave an unexpected result. Most of the 28 positive matches came from sources with a spectral index  $\alpha > -0.55$ . As this is nearly half our sample, this result points to a real (nonpulsar) source population. Using

the WISE colors, we identified that a significant fraction of these matches were likely from YSOs (X. P. Koenig & D. T. Leisawitz 2014). Radio emission from YSOs has been detected with a range of spectral indices similar to what is seen here (i.e., -0.6 to +1). This emission is thought to originate via either thermal free–free emission from ionized gas or nonthermal emission generated by jet shocks. YSOs can be time variable, with high degrees of circular polarization, and may have counterparts at X-ray, infrared, and submillimeter wavelengths (E. D. Feigelson et al. 1998; J. Forbrich et al. 2006; A. Feeney-Johansson et al. 2021). Further support for these YSO identifications came from SIMBAD and the Gaia/ALLWISE catalog of YSO candidates (G. Marton et al. 2019). All of these YSO matches are identified in Table 3 as "YSO."

Apart from YSOs associated with star formation, there is a heterogeneous collection of radio-emitting stars. For example, J165648.02-230901.8 is 24 Oph A (HD 152849), a 6th magnitude star of spectral type A05, and may be a new case of (polarized) radio emission from a rapidly rotating A star (J. A. White et al. 2021). J172055.04-272041.5 is HD 156848B, part of a spectroscopic binary (G = 9.1 mag). According to SIMBAD, one member is an F7/8 subgiant star, with the other component being either an F- or G-type star, and it is listed as a possible ROSAT source by C. B. Haakonsen & R. E. Rutledge (2009). 175920.59-301548.7 is HD 316903 and is listed in SIMBAD as a pulsating variable of spectral class B8, making it only the second  $\beta$  Cepheid variable for which radio emission has been detected (M. Tapia et al. 2014). J181952.24 -291634.4 is HD 168210, a bright (G = 8.7 mag) eclipsing binary dominated by a G5 main-sequence star. It is listed as a possible member of the nearby  $\beta$  Pictoris moving group and is a likely ROSAT source (C. B. Haakonsen & R. E. Rutledge 2009; J. Gagné et al. 2018; D. Couture et al. 2023).

There are at least three nearby M dwarfs in our sample, which appear to be fully convective according to their Gaia colors and absolute magnitudes. J170027.74–220742.7 is the high-proper-motion star 2MASS J17002789–2207322. It has the colors of a late M dwarf (M. J. Pecaut & E. E. Mamajek 2013), <sup>16</sup> and it is listed as an ultracool dwarf in the planet transit candidate survey by D. Sebastian et al. (2021). J185226.04–373037.8 is our most polarized source in the sample. J181345.72–331738.6 has been previously cataloged in SIMBAD as L489-43, a high-proper-motion M4.5 dwarf with X-ray emission (B. Riaz et al. 2006).

Our most unusual source is J180526.44–292954.6, with extreme polarization (V/I=86.3%) and spectral index  $\alpha=-4.31$ . The radio source is coincident with HD 317101A, the bright primary (G=9.9 mag) of a nearby (d=33 pc) high-propermotion (146.5 mas yr<sup>-1</sup>) visual binary system (C. A. L. Bailer-Jones et al. 2021). Based on the temperature and colors of these stars, both appear to be K dwarfs (M. J. Pecaut et al. 2012; K. G. Stassun et al. 2019). As noted in Section 6.1, HD 317101A is also an X-ray source. The radio source was observed in several MeerKAT pointings, three at or within the half-power point of the primary beam on 2020 June 28 and July 10, and each consisting of 12 5-minute scans observed over 9 hr. Images made from the combination of all 12 scans on each date vary by  $\sim$ 25% from each other.

With its strong variability, an active phase that persists for weeks or months, a high degree of polarization, and a very

 $<sup>\</sup>overline{^{16}}$  https://www.pas.rochester.edu/~emamajek/EEM\_dwarf\_UBVIJHK\_colors\_Teff.txt

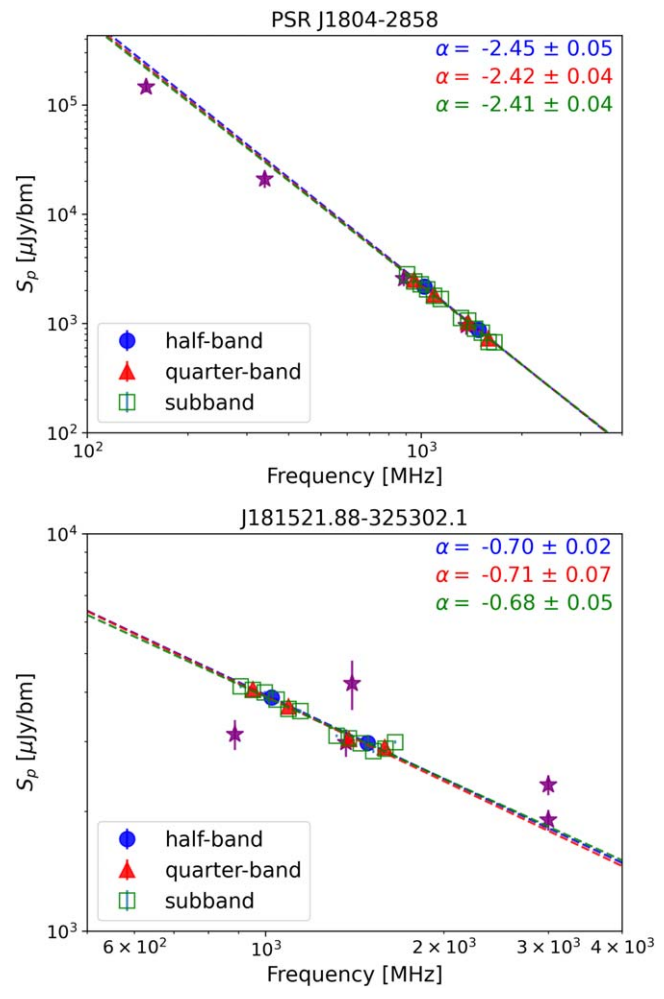


**Figure 8.** Top: spectrum of pulsar J1804–2858. Purple stars plot peak intensities from the TGSS (150 MHz, H. T. Intema et al. 2017), VLITE (340 MHz, T. E. Clarke et al. 2016), RACS-low (888 MHz, C. L. Hale et al. 2021), and RACS-mid (1368 MHz, S. W. Duchesne et al. 2023) catalogs. Blue circles, red triangles, and green squares show flux measurements from the MeerKAT half-band, quarter-band, and subband images. The corresponding inband spectral fits (dashed lines) show excellent agreement both in-band and with the other radio catalogs. Bottom: spectrum of the polarized source J181521.88–325302.1 exhibiting variability. Catalog values are from RACS-low, RACS-mid, NVSS (1.4 GHz, J. J. Condon et al. 1998), and the first two VLASS epochs (3 GHz, M. Lacy et al. 2020).

steep radio spectrum, J180526.44—292954.6 appears to share many of the characteristics of a group of GC radio transients (GCRT; S. D. Hyman et al. 2005, 2007, 2009; Z. Wang et al. 2021). However, unlike other GCRTs (e.g., J. J. Rickard & W. M. Cronyn 1979; D. L. Kaplan et al. 2008), we appear to have identified a likely multiwavelength counterpart and its distance. While time-variable, polarized radio (and X-ray) emission has been seen toward K dwarfs (M. Gudel 1992; J. Pritchard et al. 2021), the properties of this source seem extreme and are thus worthy of further study.

### 6.3. Radio Variability

In addition to pulse-to-pulse fluctuations, the flux density of pulsars can vary significantly on longer timescales owing to intrinsic effects (e.g., nulling, eclipses) and extrinsic effects (e.g., refractive and diffractive scattering). While variability was used as an early pulsar search strategy (aka "scintars";

J. J. Rickard & W. M. Cronyn 1979), and it helped to identify the first MSP (D. C. Backer et al. 1982), it has only recently been used in conjunction with other search criteria in imaging surveys (i.e., Z. Wang et al. 2021; S. Sett et al. 2023).

Our approach to studying variability was to look in existing archival surveys for radio flux density measurements of the pulsar candidates in Tables 3-5. We began first by excluding those 28 sources previously identified as stars in Section 6.2, resulting in 47 candidates. We next looked at existing archival data sets or surveys that were observed at or near the same frequency of this MeerKAT bulge data set (J. J. Condon et al. 1998; C. L. Hale et al. 2021; T. Murphy et al. 2021; S. W. Duchesne et al. 2024). Recall that our MeerKAT flux densities in Tables 3–5 were derived from the mosaic images. Although this results in fitted MeerKAT spectra with very low uncertainties, they are not useful for studying variability alone since they are time averages over multiple pointings. We consider an L-band source to be a variable source if a survey flux density differs from the MeerKAT interpolated value by more than 20% and  $3\sigma$ . This constraint yields 11 sources with 25%-60% variations based on available survey results. The circularly polarized sources J181521.88-325302.1 (shown in Figure 8) and J172329.79–282036.1 are notable examples of variability. The latter is detected at 887 MHz with a flux density of 60% and  $4\sigma$  higher than expected from the MeerKAT spectrum. Also of note is an additional 10th source, J180032.14 -273536.0, which has no survey detections but a  $5\sigma$  upper limit at 887 MHz that is 50% lower than the expected value. We include the spectrum of PSR J1804-2858 in Figure 8 to illustrate the consistency between the MeerKAT in-band measurements of the spectral index, extrapolated to archival survey measurements.

A second, less reliable measure of variability comes from comparing our results with surveys at different sky frequencies (H. T. Intema et al. 2017; N. Hurley-Walker et al. 2017, 2019; M. Lacy et al. 2020). In addition to these published surveys, we inspected the extensive database from the VLA Low-band Ionosphere and Transient Experiment (VLITE), which regularly monitors the radio sky at 340 MHz commensal with the regular observing at the Very Large Array (VLA; E. Polisensky et al. 2016; T. E. Clarke et al. 2016). In all these instances we are looking for significant deviations from the power-law fits extrapolated outside the MeerKAT band. Such deviations are less robust reliable indicators of variability since they could originate from real deviations in the pulsar's spectrum from a simple power law.

We list variable radio sources in the sixth column of Table 6. Radio sources with archival flux densities measured near or within the MeerKAT *L* band are labeled either Y1 or *N*, indicating variable or nonvariable, respectively. Note that the variability timescale is poorly constrained, as the epochs vary from months to decades. Variability outside of the MeerKAT frequency range (i.e., significant deviations from power-law extrapolations) is labeled as Y2. Sources without archival radio observations are left blank. We will discuss variability and other properties in Table 6 and in more detail in Section 7.

### 6.4. Pulsation Searches

While a case can be made that a particular source is a compelling pulsar candidate using imaging and spectra at X-ray, optical, and radio wavelengths (A. V. Karpova et al. 2023; A. Zic et al. 2024), the final arbiter is the detection of

**Table 6**Pulsar Candidate Properties

J2000 Name	Compact	Steep	C Pol.	L Pol.	Variable	HE
171334.15-241044.5	Y	N	Y	N	Y1	
172018.40-265207.8	Y	Y	Y	N		N
172329.79-282036.1	Y	Y	Y	N	Y1	N
172752.07-272724.6	Y	Y	Y	N		N
172820.26-260816.6	Y	Y	Y	N	N	
172931.96-273137.8	Y	N	Y	N		N
173250.03-235414.4	Y	N	Y	N	Y1	
173757.25-273305.3	Y	N	Y	N	N	
174006.78-280533.9	Y	N	Y	N	N	
174408.71-242453.4	Y	Y	Y	Y	Y1	
174543.03-265853.9	Y	N	Y	N	Y2	Y
174718.05-330917.4	Y	Y	Y	N	N	N
175115.97-294352.0	Y	Y	Y	N	N	
175229.06-284905.6	Y	N	Y	N	N	
175306.42-293000.8	Y	Y	Y	N	N	
175306.50-285126.2 <sup>a</sup>	Y	N	Y	N		Y
175339.01-333128.4	Y	N	Y	N	N	N
175920.04-282956.6	Y	Y	Y	N	N	
180012.33-274432.5	Y	N	Y	N		
180032.14-273536.0	Y	Y	Y	N	Y1	
180403.38-333153.0	N	N	Y	N	Y1	Y
180631.55-292137.0	Y	N	Y	N		
181137.21-320650.9	Y	N	Y	N		
181521.88-325302.1	N	N	Y	N	Y1	N
181634.34-323412.4	Y	N	Y	N		
181831.06-325418.2	Y	N	Y	N		
183449.11-350525.8	N	N	Y	N	N	N
183501.56-341820.1	Y	N	Y	N	Y2	
184154.78-360749.2	N	Y	Y	N		N
185019.66-362912.8	Y	N	Y	N	Y1	N
190625.66-370349.5	N	N	Y	N		
190738.78-370855.9	Y	N	Y	N	Y2	
170154.67-225008.3	Y	Y	N	Y		N
171837.15-233510.5	N	Y	N	Y	N	11
172626.80-304809.2	Y	Y	N	Y	N	N
173121.50-250235.7	Y	Y	N	Y	Y1	11
174408.71-242453.4	Y	Y	Y	Y	Y1	
181822.84-324416.0	Y	Y	N	Y	11	
182146.77-324727.8	N	Y	N	Y		
182417.96-323805.4	Y	Y	Y	Y		
182731.72-325238.9	Y	Y	N	Y		
183736.28-335013.8	Y	Y	N	Y		
172734.51-260957.1	Y	Y	Y	N		
173114.95-273532.4	Y	Y	Y	N N		N
180221.53-325438.0	Y	Y	Y	N N	Y1	N N
182417.96-323805.4	Y	Y	Y	Y	11	11
185120.86-354619.5	Y	N	Y	N		
103120.00-334019.3	ĭ	1N	ĭ	IN		

Note. Italics indicate the 30 candidates whose properties closely follow those of the known pulsar population.

pulsations. As a pilot project we observed three of the circularly polarized sources identified in the G0.0+5.5 mosaic pointing (J172018.40–265207.8, J172752.07–272724.6, and J172820.26–260816.6), using the Ultra-Wide Low-band (UWL; 704–4032 MHz) receiver of the Parkes 64 m radio telescope (Murriyang; G. Hobbs et al. 2020). The properties of these sources are listed in Table 3. For each source, we conducted observations using the UWL for 72 minutes, with a time resolution of 64  $\mu$ s and a frequency resolution of 0.250 MHz, corresponding to 13,312 frequency channels across the 3328 MHz UWL bandwidth. Each observation

generated approximately 200 GB of data. We conducted a pulsar search in three different ways using a GPU-accelerated search code, PEASOUP (V. Morello et al. 2019):

The maximum line-of-sight dispersion measure (DM) for these sources, based on different electron density models, ranges between 250 and 400 pc cm<sup>-3</sup> (J. M. Cordes & T. J. W. Lazio 2002; J. M. Yao et al. 2017). However, we searched over a broader DM range from 2 to 1500 pc cm<sup>-3</sup>. We first divided each UWL observation into four segments of 832 MHz bandwidth each, namely

<sup>&</sup>lt;sup>a</sup> Possibly PSR J1753-28 (see Section 6.1).

704–1536 MHz (4345 trial DMs), 1536–2368 MHz (2809 trial DMs), 2368–3200 MHz (1570 trial DMs), and 3200–4032 MHz (853 trial DMs). We then conducted a standard fast Fourier transform search separately for each segment. Candidates with a spectral S/N above 6 were folded using dspsr, and diagnostic plots were obtained using PSRCHIVE's tool pdmp (W. van Straten & M. Bailes 2011; W. van Straten et al. 2012). After folding, candidates with a folded S/N above 8.5 were selected for visual inspection. However, we did not find any significant candidate resembling a real pulsar.

- 2. We also conducted an acceleration search for the same data set. The acceleration range searched was from -30 to +30 ms<sup>-2</sup> (which is consistent with the maximum acceleration shown by the majority of the known binary pulsars during 1 hr integration), and the DM range was 2-500 pc cm<sup>-3</sup>. We folded all candidates with a spectral S/N above 7 and visually inspected each with folded S/N above 8.5, but this search also did not yield any significant candidates.
- 3. Furthermore, we divided the UWL observations into smaller segments, each with a bandwidth of 416 MHz, and conducted an acceleration search similar to that mentioned in step 2. This search also did not detect any candidates.

#### 7. Results

#### 7.1. Pulsar Candidates

We have identified a sample of 75 polarized sources in a MeerKAT imaging survey of the bulge of our Galaxy. A total of 60 were found based on their circular polarization (Section 5.2), 10 were found from their linear polarization properties (Section 5.3), and 5 were steep-spectrum polarized sources, detected only in the lower half of the MeerKAT receivers (Section 5.4). We searched for multiwavelength counterparts to each of these candidates at gamma- and X-ray energies (Section 6.1), plus optical and infrared wavelengths (Section 6.2). Based on optical/infrared identifications, we found that 28 of the circular polarized sources were bright stars or YSOs. Removing these, our final list is shown in the Boolean Table 6. After accounting for duplicates that were detected in both linear and circular polarization, we have a total of 45 sources taken from Tables 3–5.

Table 6 lists several source properties common to previous image-based searches for pulsars: compactness, spectral steepness, circular polarization, linear polarization, variability, and high-energy counterparts. Measures that define how pointlike a radio source is, such as the ratio of the total flux over the peak flux density (e.g., D. A. Frail et al. 2018) or the compactness ratio, as defined in Section 4 (H. T. Intema et al. 2017), have proven useful in identifying pulsar candidates. Despite being unresolved in interferometric images, F. de Gasperin et al. (2018) noted that pulsars may still have compactness less than unity (but usually >0.9). This occurs if there are substantial flux density changes within an integration period (scintillation or pulse-to-pulse variations), or the pulsar is located near extended emission (e.g., pulsar wind nebulae). In all cases, even the noncompact sources in Table 6 have a total flux over the peak flux density ratio R < 1.5, i.e., they meet the compactness criteria used in S. D. Hyman et al. (2019) and elsewhere. For spectral steepness we have assigned "Y" to those with  $\alpha < -1.5$  (see Section 5.3), the circular and linear

polarization criteria are defined in Sections 5.2–5.4, and variability is defined in Section 6.3. Finally, we identify all candidates with high-energy counterparts (Section 6.1). Unlike the eRosita catalog, which covers the entire 4th Galactic quadrant, sky coverage of the Chandra catalog is patchy enough that sources in the first Galactic quadrant often lack sufficient data to rule out X-ray emission.

Of these 45 polarized sources, there are two sources (J174408.71–242453.4 and J182417.96–323805.4) that are notable for being compact, having a steep spectrum, and being detected with both strong circular and linear polarization (>10%). Pulsars are the only known compact source population with steep radio spectra to exhibit strong polarization in both forms. These would be high-priority candidates for follow-up pulsation searches. Approximately half of our candidates (22) in Table 6 are compact, have a steep spectrum, and have linear or circular polarization. With a few exceptions, which we discuss below, the bulk of these sources also appear to be attractive candidates for pulsation follow-up.

Five polarized sources (including J174408.71–242453.4) are compact, have a steep spectrum, and exhibit strong in-band variability (Y1; see Section 6.3). These warrant special attention in pulsation follow-up. The remaining variable sources have a flat spectrum and are likely stellar sources. The three high-energy counterpart associations are less instructive than the other indicators. In Section 6.1 we suggest that one source (J175306–285126.2) may be a known pulsar, while the remaining two have flat spectral indices similar to the YSOs identified in Section 6.2.

Despite our best efforts at using these multiple selection criteria to select pulsars, there likely remain other source populations among our 45 polarized sources. To illustrate this, we plot the spectral index versus the absolute value of the circular polarization in Figure 9. On the left are the known pulsars (blue) from Table 2 together with the stars (green) identified from Section 6.2. The light-gray points are circular polarization and spectral index values taken from the compilations of S. Johnston & M. Kerr (2018) and F. Jankowski et al. (2018), respectively. The known bulge pulsars trace the spectral index and circular polarization of this larger pulsar sample, except that the larger sample extends to less steep spectral indices and larger polarization (≤40%). It is clear that the majority of stars occupy a different phase space in this diagram. They are distributed over nearly the full range of circular polarization, and most have distinctively flat or inverted spectral indices.

In the right panel of Figure 9 we plot the remaining 45 polarized sources (red) from Table 6. Compared to the larger sample of pulsars (light gray), there is an excess of flat-spectrum candidates in the 1%-2% range and a long tail of strongly polarized sources (>50%). We discussed the excess of bright sources in the 1%-2% range in Section 5.2. With the exception of J180221.53-325438.0 with  $\alpha=-1.61$ , we suspect that the remaining are extragalactic sources with weak circular polarization or beam squint artifacts.

The long tail of strongly polarized sources (>40%) in Figure 9 is likely real and not a selection effect or instrumental artifact. Unless there is a pulsar emission geometry that results in a high percentage polarization while making pulsations difficult to detect (i.e., aligned rotators), the bulk of this sample is likely stellar in origin. Many radio stars at this frequency exhibit high fractional circular polarization (J. Pritchard et al. 2021, 2024), with properties similar to the stars identified in

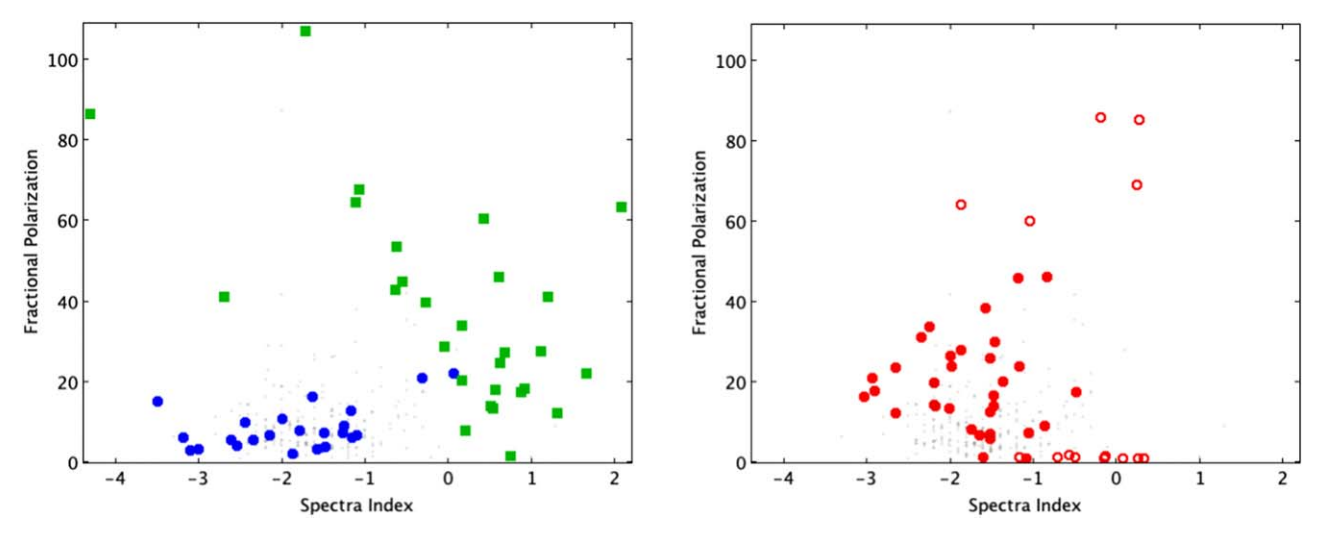


Figure 9. Left: circular polarization and spectral properties of known pulsars (blue circles) and stars (green squares) identified in Tables 2 and 3. Gray points are taken from the compilation of circular polarization and spectral index values of S. Johnston & M. Kerr (2018) and F. Jankowski et al. (2018). Right: polarization (circular and linear) vs. spectral Index for pulsar candidates (red) identified in Table 6. Filled (open) circles represent candidates that lie inside (outside) the known pulsar distribution. The light-gray points are the same as the adjacent plot.

Table 3 and Figure 9. What is rarer are stellar radio stars whose spectral indices are comparable to those of pulsars and suggest a coherent process such as electron cyclotron maser emission (M. Güdel 2002). Improved astrometry of these steepspectrum, highly polarized candidates will help in identifying multiwavelength counterparts to show whether they are similar to the peculiar J180526.44-292954.6 (Section 6.2) or remain interesting pulsar candidates. If we confine the source selection to just those candidates with fractional polarization between 1% and 45% and a negative spectral index, consistent with known pulsar properties, we are left with 30 strong pulsar candidates. The J2000 names of these candidates are highlighted in italics in Table 6. We note that the excess of positive V sources first discussed in Section 5.1 persists in each of these subsamples. In addition, for the nonpulsar populations (e.g., YSOs) a positively circularly polarized source is just as likely to have a multiwavelength counterpart as a negatively polarized source. The implications of this result are discussed further in Section 5.1.

To summarize, of the 45 candidates in Table 6 that were initially identified on the basis of multiple selection criteria (compactness, spectral index, polarization, variability, and multiwavelength counterparts), we find 30 whose properties closely follow those of the known pulsar population and are thus good candidates for pulsation follow-up.

#### 7.2. Summary of the Candidate Selection Process

Since this search has been a multistep process, it is useful to summarize the major steps that have led to a final list of promising pulsar candidates in Section 7.1. We began with a set of 20 full Stokes images of a 173  $\deg^2$  vertical strip of the Galactic bulge. Within this region we identified 387,875 unique radio sources with Stokes *I* flux density. For each of these sources we measured values (or limits) of Stokes *Q*, *U*, and *V* and in-band spectral indices.

To test the efficacy of our methods, we used this catalog to generate a list of the known pulsars that were present in the source catalog. We found polarized emission (linear and circular) from 39 of the 81 known pulsars that lie within this survey area (Table 2).

As a first step in the selection process, we identified 353 circularly polarized sources above  $5\sigma$ . Bright Stokes I sources with |V/I| < 1% were eliminated from this sample as likely beam squint artifacts, leaving 100 circularly polarized sources. From visual inspection of the images we identified another 38 likely image artifacts (e.g., sidelobe contamination). After removing the known pulsars, we were left with 60 circularly polarized sources (Table 3).

A similar method was followed to identify linearly polarized sources, but owing to high source density in the linearly polarized images, there was a much greater incidence of artifacts. As a result, additional selection criteria were required (compactness, spectral index, and fractional polarization) to keep the false positives to a manageable level. After removing likely artifacts, the final sample has 10 linearly polarized sources (Table 4). As a final method, we confined our search to polarized sources in the lower half of the MeerKAT band to catch fainter, steep-spectrum sources missed in our full-band searches. This resulted in five additional circularly polarized sources (Table 5). In total, these searches resulted in 75 polarized sources (Tables 3–5).

The next step in the selection process was to search for multiwavelength counterparts of our polarized sources. We identified 28 bright stellar sources (YSOs, M stars, pulsating variable, etc.) with high confidence. After removing these sources and accounting for two duplicate sources that were both circularly and linearly polarized, we are left with a sample of 45 polarized sources. While all of these are viable pulsar candidates, it is clear from their aggregate properties that there still remain nonpulsars or pulsar outliers in this sample. To further refine this polarized sample, we examine other known pulsar properties, including compactness, spectrum, variability, and high-energy counterparts. A final list of 30 promising candidates (italic source names in Table 6) is obtained by requiring that these source properties are in line with known pulsars.

## 7.3. The Missing Pulsations

There are 81 pulsars that have been previously discovered toward these bulge mosaic fields (Section 5.1). In this work we have identified 30 additional pulsar candidates. The immediate

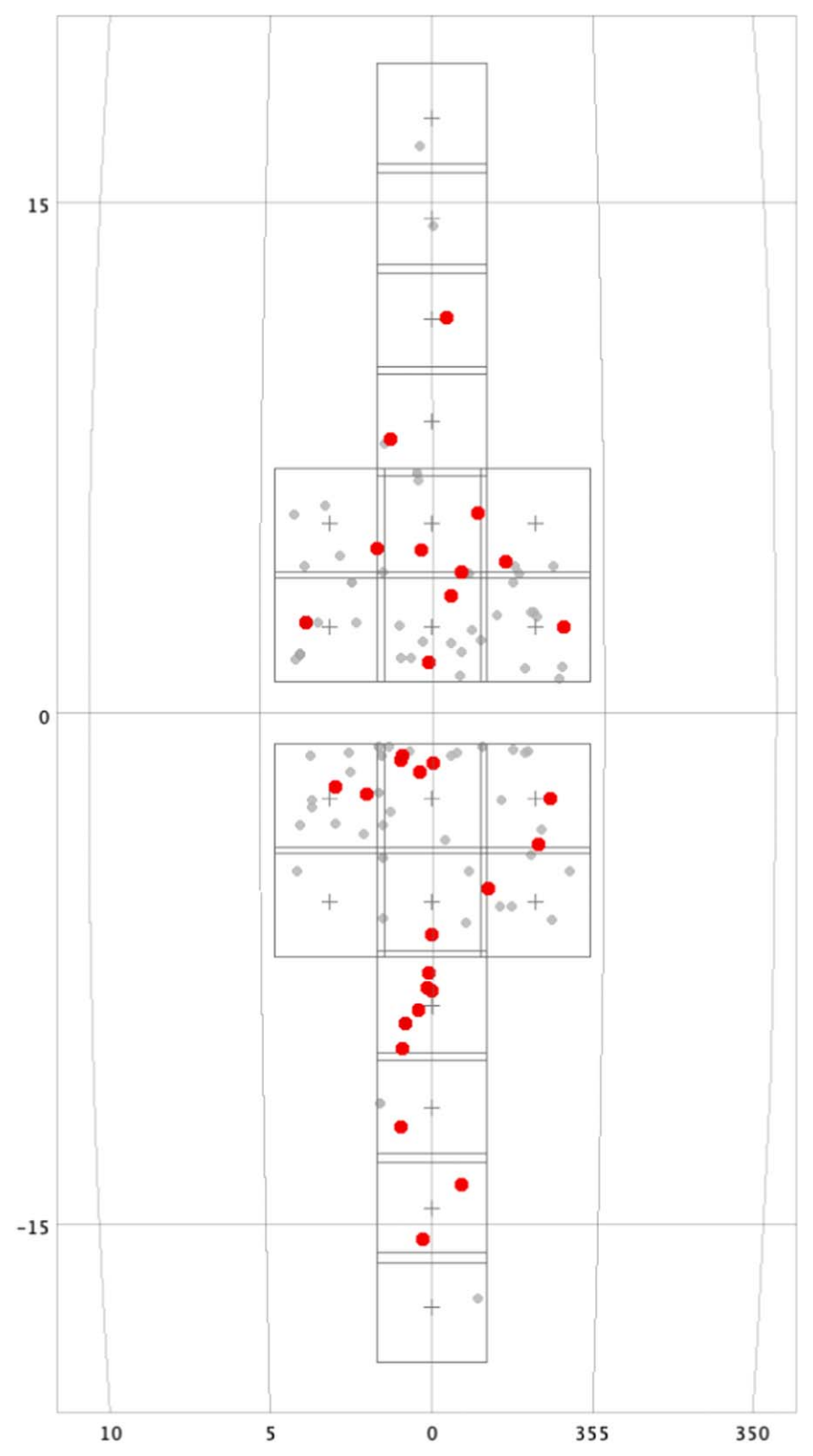


Figure 10. Galactic distribution of the known pulsars in the mosaic fields (light-gray circles) vs. our final 30 pulsar candidates (red circles).

question that needs to be answered is, why have previous pulsation searches, including Section 6.4, not detected pulsations toward these sources? A myriad of reasons for nondetection of pulsations have been previously discussed in the literature and broadly fall into four categories: instrumental, algorithmic, environmental, and intrinsic. The challenges and

strategies for finding pulsations toward the bulge and the GC have been discussed extensively (J.-P. Macquart & N. Kanekar 2015; F. Calore et al. 2016; S. D. Hyman et al. 2019, 2021).

Instrumental sensitivity appears to be part of the explanation. The deepest pulsation surveys at 1.4 GHz that cover the MeerKAT bulge mosaic images are the Parkes High Time

Resolution Universe (HTRU) survey (M. J. Keith et al. 2010) and the Parkes Multi-beam Pulsar Survey (PMPS; R. N. Manchester et al. 2001). The majority of the known 81 pulsars were discovered by the PMPS and the HTRU survey. Thanks to improvements in search algorithms, the reprocessing of these data sets has led to additional new pulsar discoveries close to the continuum sensitivity limits (A. D. Cameron et al. 2020; R. Sengar et al. 2023)

The PMPS surveyed  $|b| < 5^{\circ}$ , while the HTRU survey had three parts: HTRU-low with  $|b| < 3^{\circ}.5$ , HTRU-mid with  $|b| < 15^{\circ}$ , and HTRU-high for all other Galactic latitudes. The integration time at the low, mid-, and high latitudes was 4300 s (twice the PMPS), 540 s, and 270 s, respectively. The HTRU survey had smaller channel bandwidths than the PMPS, making it less limited by dispersion and scattering, thus increasing its sensitivity to distant MSPs. The mean limiting flux density of the HTRU has a strong latitude dependence in part because of the decreasing integration times from low to mid- to high, but also because of the variation in sky temperature (M. R. Calabretta et al. 2014; M. Remazeilles et al. 2015). Taken together, we estimate that the HTRU-high and HTRU-mid were  $3.5 \times$  and  $2.6 \times$  less sensitive than the HTRU-low, respectively.

In contrast, the rms noise for the MeerKAT bulge mosaic images does not show a strong Galactic latitude dependence. The noise is relatively constant with a mean of 14  $\mu$ Jy beam<sup>-1</sup> (see Table 1), varying by  $\sim 30\%$  owing to changes in  $T_{\rm sky}$  and varying degrees of RFI. Using the radiometer equation and the instrumental parameters of the HTRU survey for the outer beams of the 13-beam receiver (M. J. Keith et al. 2010; A. D. Cameron et al. 2020), we expect the limiting flux density of the MeerKat polarized pulsar candidates to be very similar to that of pulsars previously seen by HTRU-low. This indeed appears to be the case. We find that the limiting flux density for both the HTRU detections and the circularly polarized candidates in Tables 3 and 5 is approximately 0.1 mJy. Since our pulsar candidates are distributed over  $|b| < 20^{\circ}$  (see Figure 10), the sharp decrease in the HTRU sensitivity with latitude likely explains why the fainter pulsar candidates were missed in previous pulsation searches.

Sensitivity cannot explain why the HTRU survey previously did not detect pulsations from the brighter candidates, such as J174408.71-242453.4, a 1.2 mJy source that is compact, has a steep spectrum, and has both significant linear and circular polarization. The sky distribution of our sample, compared to existing pulsation surveys, offers some clues (Figure 10). There are two groupings of candidates in the mosaic fields: a group of seven distributed along a narrow band of longitude primarily in the G0.0-8.5 mosaic, and a less well-defined group near  $b=5^{\circ}$ . While this clustering could be random, we note that they occur in the direction of "voids" wherein there are no known pulsars. We suggest that anomalous scattering might be responsible for one or more of these voids. An excellent case in point is the recent discovery of the highly scattered pulsar PSR J1032–5804 from an imaging survey of polarized sources (Z. Wang et al. 2024).

If sensitivity and interstellar scattering are the main culprits, then deeper searches and/or searches above L band should be successful in detecting pulsations. Neither of these appears to explain the lack of pulsations from the three candidates observed in Section 6.4. The search of these midlatitude candidates was conducted with the Parkes telescope using the same integration time as HTRU-low, over a much wider frequency range

(704-4032 MHz), and using state-of-the-art search algorithms. Using the instrumental parameters from Section 6.4 and  $T_{\rm sky}$  at the source positions, we used the radiometer equation to calculate the rms noise. The resulting the radiometer equation to calculate the rms noise. The resulting the radiometer equation to calculate the rms noise. The resulting the radiometer equation to calculate the rms noise. 6.7 K, a bandwidth of 1024 MHz, and an S/N threshold of 8.5, the sensitivity is 0.1 mJy  $\times \sqrt{w_t/(P-w_t)}$ , where P is the pulsar period and  $w_t$  is the quadrature sum of the intrinsic pulsar width, temporal scattering, dispersive smearing, and sampler timescale (R. Sengar et al. 2023). We then modeled an isolated MSP with  $P \sim 5$  ms with a 5%–10% pulse width at a distance of 8300 pc, estimating its DM and the degree of scattering using two Galactic electron density models (J. M. Cordes & T. J. W. Lazio 2002; J. M. Yao et al. 2017). We find that pulsations should have been expected for this putative bulge MSP at high significance over much of the frequency range of the UWL receiver. Perhaps some of the candidates are rare and more exotic systems such as tight binaries or pulsars with broad emission profiles (J. Navarro et al. 1995; D. L. Kaplan et al. 2019), or, as has been suggested, represent a new galactic population with properties like pulsars but lacking pulsations (S. D. Hyman et al. 2021).

#### 8. Discussion and Conclusions

We have carried out an analysis of a sensitive MeerKAT survey of the Galactic bulge and GC region at L band (856–1712 MHz) in all four Stokes I, Q, U, and V images. The survey covers  $173 \, \mathrm{deg}^2$  in 20 partially overlapping mosaic pointings, each  $3^\circ.125 \times 3^\circ.125$ . Our primary science driver has been to identify pulsar candidates, with a long-term goal of explaining the origin of the mysterious gamma-ray emission identified by the Fermi Gamma-Ray Telescope.

Previous image-based candidate searches have been plagued by contaminants (variables, extragalactic sources, etc.; e.g., C. De Breuck et al. 2000; D. L. Kaplan et al. 2000; D. A. Frail et al. 2018; F. de Gasperin et al. 2018; Y. Maan et al. 2018; S. Bruzewski et al. 2023). This current work is a substantial improvement over past image-based pulsar searches in several dimensions: sensitivity, improved angular resolution/astrometry, polarization, in-band spectra, and the use of multiple selection criteria. The rms noise levels of these mosaic images are  $12-17~\mu Jy~ba^{-1}$  (see Table 1). When past continuum surveys such as the NRAO VLA Sky Survey (NVSS; J. J. Condon et al. 1998), the TIFR GMRT Sky Survey (TGSS; H. T. Intema et al. 2017), and the Galactic and Extragalactic All-sky Murchison Widefield Array (MWA) survey (GLEAM; N. Hurley-Walker et al. 2017) are scaled to L band, using a mean pulsar spectral index, this MeerKAT bulge survey has an increase in sensitivity of nearly two orders of magnitude. Using the MeerKAT Absorption Line Survey (MALS; P. P. Deka et al. 2024), M. D. Himes et al. (2024, in preparation) showed that these earlier surveys were sensitive to between 7% and 21% of the known pulsar population, while for MALS the fraction was 80%. The same conclusion applies to this MeerKAT bulge survey since it is approximately a factor of two deeper than MALS. More importantly, for the first time the continuum sensitivity has reached a level that is capable of detecting the putative population of MSPs in the Galactic bulge, which can be responsible for the Fermi excess and whose properties have been described by F. Calore et al. (2016).

<sup>17</sup> https://www.parkes.atnf.csiro.au/cgi-bin/utilities/pks\_sens.cgi

The next generation of all-sky surveys capable of imaging the GC and bulge will have sensitivities comparable to MeerKAT. One area where MeerKAT retains an advantage over ASKAP (T. Murphy et al. 2021; Z. Wang et al. 2022b) and MWA (N. Hurley-Walker et al. 2022) is in angular resolution. Higher resolution can be useful for identifying false positives such as extended, steep-spectrum, high-redshift galaxies (G. Miley & C. De Breuck 2008), but for a crowded region such as the bulge, accurate astrometry is essential to identify multiwavelength counterparts (Section 6).

Another improved capability of these next-generation facilities is the ability to provide full Stokes images. At these sensitivity levels, just using criteria such as compactness and spectral index (e.g., D. L. Kaplan et al. 2000; F. de Gasperin et al. 2018; Y. Maan et al. 2018) produces too many candidates. For example, if we select all compact and steep spectral index sources in the G0.0+5.5 mosaic using the criteria in Section 5.3, we find nearly 900 candidates, or nearly 4% of the cataloged radio sources for a source density of 90 deg<sup>-2</sup>. Including a polarization criterion for this sample (Section 5.2) sharply reduces this source density. For this bulge survey region, if we include the known pulsars in Table 2 and the circularly polarized candidates in Tables 3 and 5, the source density drops to a manageable 0.5 deg<sup>-2</sup>.

The large fractional bandwidths allow for the measurement of the spectral index at one time, reducing the rate of false positives. Past searches determined the spectral index from two or more surveys at different frequencies but often taken at very different epochs (e.g., D. A. Frail et al. 2016; A. V. McCarver et al. 2024). F. de Gasperin et al. (2018) argued that the tail of the spectral index distribution at the steep end could be contaminated by variable extragalactic sources. To our knowledge, this is the first large-scale study to identify pulsar candidates using both spectral indices and polarization. As we showed in Section 7.1, the polarization/spectral index space (Figure 9) can be a powerful tool for distinguishing different source populations. As an added benefit, this method should allow us to identify promising pulsar candidates without restricting the search to the steepest spectral indices. Finally, we note that this work has followed the recent trend of using multiple selection criteria (variability, compactness, steepspectrum, polarization, and multiwavelength counterparts) to bolster claims of pulsar candidates (S. Sett et al. 2023).

After applying these selection criteria, we identify 45 pulsar candidates (Section 7.1). We noted that there likely remained some false positives in the sample, due in part to instrumental artifacts at low fractional polarization (1%–2%) and the difficulty in identifying optical/infrared counterparts in these crowded GC fields with our current astrometric accuracy (Section 4.1). Focusing on just those that have observational properties similar to the known pulsars, we find 30 strong candidates for pulsation follow-up. We argue that the absence of pulsations from these candidates from previous surveys is mainly due to a combination of low sensitivity and interstellar scattering, but other factors must be involved.

The challenges facing pulsation searches in the Galactic bulge are demonstrated by the recent discovery of the first MSP close to the GC. X-ray and radio images showed a compact source embedded within a faint filament west of the well-known nonthermal source G359.1–0.2 (the "Snake"), but it took a targeted search to find PSR J1744–2946 with a period  $P = 8.4 \,\mathrm{ms}$  (M. E. Lower et al. 2024). The pulsar was visible

on MeerKAT images at 1.4 GHz, but its pulses were scatter broadened, while the same pulses were bright at 2.1 GHz (0.43 mJy). This explains why it was missed by the HTRU survey and highlights the importance of wide-bandwidth searches. If PSR J1744–2946 is located within the Galactic bulge, it may lie on the high-luminosity tail of the putative bulge pulsar population discussed by F. Calore et al. (2016). This conclusion also applies to the pulsar candidates identified here because our polarization criterion limits detection to  $\gtrsim$ 0.1 mJy. In order to exploit the full power of these sensitive Stokes *I* MeerKAT observations in image-based pulsar searches, other multiwavelength approaches based on cross-correlation techniques may be needed (J. Berteaud et al. 2023, 2024, in preparation).

# Acknowledgments

The MeerKAT telescope is operated by the South African Radio Astronomy Observatory, which is a facility of the National Research Foundation, an agency of the Department of Science and Innovation. Murriyang, the Parkes radio telescope, is part of the Australia Telescope National Facility, which is funded by the Australian Government for operation as a National Facility managed by CSIRO. The National Radio Astronomy Observatory is a facility of the National Science Foundation operated under cooperative agreement by Associated Universities, Inc. This work has made use of data from the European Space Agency (ESA) mission Gaia (https:// www.cosmos.esa.int/gaia), processed by the Gaia Data Processing and Analysis Consortium (DPAC, https://www. cosmos.esa.int/web/gaia/dpac/consortium). Funding for the DPAC has been provided by national institutions, in particular the institutions participating in the Gaia Multilateral Agreement. R.S. and D.K. are supported by NSF grant AST-1816904. Parts of the results in this work make use of the color maps in the CMasher package (E. van der Velden 2020). Basic research at NRL is funded by 6.1 Base programs. This project was supported in part by an appointment to the NRC Research Associateship Program at the US Naval Research Laboratory, administered by the Fellowships Office of the National Academies of Sciences, Engineering, and Medicine.

Facilities: MeerKAT, Parkes.

Software: PyBDSF (N. Mohan & D. Rafferty 2015), astropy (Astropy Collaboration et al. 2013, 2018), TOPCAT (M. B. Taylor 2005; M. Taylor 2011),

#### **ORCID iDs**

Dale A. Frail https://orcid.org/0009-0008-7604-003X Emil Polisensky https://orcid.org/0000-0003-3272-9237 Scott D. Hyman https://orcid.org/0009-0006-5070-6329 William D. Cotton https://orcid.org/0000-0001-7363-6489 Namir E. Kassim https://orcid.org/0000-0001-8035-4906 Michele L. Silverstein https://orcid.org/0000-0003-2565-7909 Rahul Sengar https://orcid.org/0000-0002-9409-3214 David L. Kaplan https://orcid.org/0000-0001-6295-2881 Francesca Calore https://orcid.org/0000-0001-7722-6145 Joanna Berteaud https://orcid.org/0000-0003-4962-145X Maïca Clavel https://orcid.org/0000-0003-0724-2742 Marisa Geyer https://orcid.org/0000-0002-2822-1919 Samuel Legodi https://orcid.org/0000-0001-5205-8501 Vasaant Krishnan https://orcid.org/0000-0002-1966-5729 Sarah Buchner https://orcid.org/0000-0002-1691-0215 Fernando Camilo https://orcid.org/0000-0002-1873-3718

#### References

```
Abbate, F., Ridolfi, A., Freire, P. C. C., et al. 2023, A&A, 680, A47
Abdollahi, S., Acero, F., Baldini, L., et al. 2022, ApJS, 260, 53
Anna-Thomas, R., Burke-Spolaor, S., Law, C. J., et al. 2024, ApJ, 974, 72
Antoniadis, J. 2021, MNRAS, 501, 1116
Anumarlapudi, A., Ehlke, A., Jones, M. L., et al. 2023, ApJ, 956, 28
Astropy Collaboration, Price-Whelan, A. M., Sipőcz, B. M., et al. 2018, AJ,
   156, 123
Astropy Collaboration, Robitaille, T. P., Tollerud, E. J., et al. 2013, A&A,
  558, A33
Backer, D. C., Kulkarni, S. R., Heiles, C., Davis, M. M., & Goss, W. M. 1982,
   Natur, 300, 615
Bahramian, A., Heinke, C. O., Kennea, J. A., et al. 2021, MNRAS, 501, 2790
Bailer-Jones, C. A. L., Rybizki, J., Fouesneau, M., Demleitner, M., &
   Andrae, R. 2021, AJ, 161, 147
Ballet, J., Bruel, P., Burnett, T. H., Lott, B. & The Fermi-LAT collaboration
   2023, arXiv:2307.12546
Berteaud, J., Calore, F., Clavel, M., et al. 2021, PhRvD, 104, 043007
Berteaud, J., Calore, F., Clavel, M., et al. 2023, EPJWC, 280, 09003
Bhakta, D., Deneva, J. S., Frail, D. A., et al. 2017, MNRAS, 468, 2526
Bruzewski, S., Schinzel, F. K., & Taylor, G. B. 2023, ApJ, 943, 51
Calabretta, M. R., Staveley-Smith, L., & Barnes, D. G. 2014, PASA,
  31, e007
Callingham, J. R., Shimwell, T. W., Vedantham, H. K., et al. 2023, A&A,
  670, A124
Calore, F., Di Mauro, M., Donato, F., Hessels, J. W. T., & Weniger, C. 2016,
   ApJ, 827, 143
Calore, F., Donato, F., & Manconi, S. 2021, PhRvL, 127, 161102
Cameron, A. D., Champion, D. J., Bailes, M., et al. 2020, MNRAS, 493, 1063
Camilo, F., Scholz, P., Serylak, M., et al. 2018, ApJ, 856, 180
Cantat-Gaudin, T., & Brandt, T. D. 2021, A&A, 649, A124
Charlot, P., Jacobs, C. S., Gordon, D., et al. 2020, A&A, 644, A159
Clarke, T. E., Kassim, N. E., Brisken, W., et al. 2016, Proc. SPIE, 9906,
   99065B
Condon, J. J., Cotton, W. D., Greisen, E. W., et al. 1998, AJ, 115, 1693
Cordes, J. M., & Lazio, T. J. W. 2002, arXiv:astro-ph/0207156
Cotton, W. D., Filipović, M. D., Camilo, F., et al. 2024, MNRAS, 529, 2443
Couture, D., Gagné, J., & Doyon, R. 2023, ApJ, 946, 6
Cui, B. Y., Boyles, J., McLaughlin, M. A., & Palliyaguru, N. 2017, ApJ, 840, 5
De Breuck, C., van Breugel, W., Röttgering, H. J. A., & Miley, G. 2000,
    &AS, 143, 303
de Gasperin, F., Intema, H. T., & Frail, D. A. 2018, MNRAS, 474, 5008
Deka, P. P., Gupta, N., Jagannathan, P., et al. 2024, ApJS, 270, 33
Duchesne, S. W., Grundy, J. A., Heald, G. H., et al. 2024, PASA, 41, e003
Duchesne, S. W., Thomson, A. J. M., Pritchard, J., et al. 2023, PASA, 40, e034
Evans, I. N., Primini, F. A., Glotfelty, K. J., et al. 2010, ApJS, 189, 37
Feeney-Johansson, A., Purser, S. J. D., Ray, T. P., et al. 2021, A&A,
   653, A101
Feigelson, E. D., Carkner, L., & Wilking, B. A. 1998, ApJL, 494, L215
Forbrich, J., Preibisch, T., & Menten, K. M. 2006, A&A, 446, 155
Frail, D. A., Jagannathan, P., Mooley, K. P., & Intema, H. T. 2016, ApJ,
   829, 119
Frail, D. A., Ray, P. S., Mooley, K. P., et al. 2018, MNRAS, 475, 942
Gagné, J., Mamajek, E. E., Malo, L., et al. 2018, ApJ, 856, 23
Gaia Collaboration, Brown, A. G. A., Vallenari, A., et al. 2021, A&A, 649, A1
Gaia Collaboration, Vallenari, A., Brown, A. G. A., et al. 2023, A&A, 674, A1
George, S. J., Stil, J. M., & Keller, B. W. 2012, PASA, 29, 214
Goedhart, S., Cotton, W. D., Camilo, F., et al. 2024, MNRAS, 531, 649
Gudel, M. 1992, A&A, 264, L31
Güdel, M. 2002, ARA&A, 40, 217
Haakonsen, C. B., & Rutledge, R. E. 2009, ApJS, 184, 138
Hale, C. L., McConnell, D., Thomson, A. J. M., et al. 2021, PASA, 38, e058
Heywood, I. 2023, MNRAS, 525, L76
Heywood, I., Rammala, I., Camilo, F., et al. 2022, ApJ, 925, 165
Hobbs, G., Manchester, R. N., Dunning, A., et al. 2020, PASA, 37, e012
Hurley-Walker, N., Callingham, J. R., Hancock, P. J., et al. 2017, MNRAS,
   464, 1146
Hurley-Walker, N., Galvin, T. J., Duchesne, S. W., et al. 2022, PASA, 39, e035
Hurley-Walker, N., Hancock, P. J., Franzen, T. M. O., et al. 2019, PASA,
Hyman, S. D., Frail, D. A., Deneva, J. S., et al. 2019, ApJ, 876, 20
Hyman, S. D., Frail, D. A., Deneva, J. S., et al. 2021, MNRAS, 507, 3888
Hyman, S. D., Lazio, T. J. W., Kassim, N. E., et al. 2005, Natur, 434, 50
Hyman, S. D., Roy, S., Pal, S., et al. 2007, ApJL, 660, L121
Hyman, S. D., Wijnands, R., Lazio, T. J. W., et al. 2009, ApJ, 696, 280
```

```
598, A78
Jankowski, F., van Straten, W., Keane, E. F., et al. 2018, MNRAS, 473, 4436
Johnston, S., & Kerr, M. 2018, MNRAS, 474, 4629
Jonas, J. & MeerKAT Team 2016, in MeerKAT Science: On the Pathway to
   the SKA (Trieste: SISSA), 1
Jonker, P. G., Bassa, C. G., Nelemans, G., et al. 2011, ApJS, 194, 18
Jonker, P. G., Torres, M. A. P., Hynes, R. I., et al. 2014, ApJS, 210, 18
Kaplan, D. L., Cordes, J. M., Condon, J. J., & Djorgovski, S. G. 2000, ApJ,
   529, 859
Kaplan, D. L., Dai, S., Lenc, E., et al. 2019, ApJ, 884, 96
Kaplan, D. L., Hyman, S. D., Roy, S., et al. 2008, ApJ, 687, 262
Karpova, A. V., Zyuzin, D. A., Shibanov, Y. A., & Gilfanov, M. R. 2023,
   MNRAS, 524, 3020
Keith, M. J., Jameson, A., Van Straten, W., et al. 2010, MNRAS, 409, 619
Knowles, K., Cotton, W. D., Rudnick, L., et al. 2022, A&A, 657, A56
Koenig, X. P., & Leisawitz, D. T. 2014, ApJ, 791, 131
Koljonen, K. I. I., & Linares, M. 2023, MNRAS, 525, 3963
Lacy, M., Baum, S. A., Chandler, C. J., et al. 2020, PASP, 132, 035001
LaRosa, T. N., Kassim, N. E., Lazio, T. J. W., & Hyman, S. D. 2000, AJ,
   119, 207
Lazio, T. J. W., & Cordes, J. M. 2008, ApJS, 174, 481
Lenc, E., Murphy, T., Lynch, C. R., Kaplan, D. L., & Zhang, S. N. 2018,
    MNRAS, 478, 2835
Livingston, J. D., McClure-Griffiths, N. M., Gaensler, B. M., Seta, A., &
   Alger, M. J. 2021, MNRAS, 502, 3814
Lower, M. E., Dai, S., Johnston, S., & Barr, E. D. 2024, ApJL, 967, L16
Maan, Y., Bassa, C., van Leeuwen, J., Krishnakumar, M. A., & Joshi, B. C.
   2018, ApJ, 864, 16
Macquart, J.-P. 2002, PASA, 19, 43
Macquart, J.-P., & Kanekar, N. 2015, ApJ, 805, 172
Manchester, R. N., Hobbs, G. B., Teoh, A., & Hobbs, M. 2005, AJ, 129, 1993
Manchester, R. N., Lyne, A. G., Camilo, F., et al. 2001, MNRAS, 328, 17
Marton, G., Abraham, P., Szegedi-Elek, E., et al. 2019, MNRAS, 487, 2522
Mauch, T., Cotton, W. D., Condon, J. J., et al. 2020, ApJ, 888, 61
McCarver, A. V., Maccarone, T. J., Ransom, S. M., et al. 2024, ApJ, 969, 30
Merloni, A., Lamer, G., Liu, T., et al. 2024, A&A, 682, A34
Miley, G., & De Breuck, C. 2008, A&ARV, 15, 67
Mohan, N., & Rafferty, D., 2015 PyBDSF: Python Blob Detection and Source
   Finder, Astrophysics Source Code Library, ascl:1502.007
Morello, V., Barr, E. D., Cooper, S., et al. 2019, MNRAS, 483, 3673
Muno, M. P., Bauer, F. E., Bandyopadhyay, R. M., & Wang, Q. D. 2006,
   ApJS, 165, 173
Murgia, S. 2020, ARNPS, 70, 455
Murphy, T., Kaplan, D. L., Stewart, A. J., et al. 2021, PASA, 38, e054
Navarro, J., de Bruyn, A. G., Frail, D. A., Kulkarni, S. R., & Lyne, A. G. 1995,
   ApJL, 455, L55
Nord, M. E., Lazio, T. J. W., Kassim, N. E., et al. 2004, AJ, 128, 1646
Pecaut, M. J., & Mamajek, E. E. 2013, ApJS, 208, 9
Pecaut, M. J., Mamajek, E. E., & Bubar, E. J. 2012, ApJ, 746, 154
Polisensky, E., Lane, W. M., Hyman, S. D., et al. 2016, ApJ, 832, 60
Possenti, A., Cerutti, R., Colpi, M., & Mereghetti, S. 2002, A&A, 387, 993
Pritchard, J., Murphy, T., Heald, G., et al. 2024, MNRAS, 529, 1258
Pritchard, J., Murphy, T., Zic, A., et al. 2021, MNRAS, 502, 5438
Remazeilles, M., Dickinson, C., Banday, A. J., Bigot-Sazy, M.-A., &
   Ghosh, T. 2015, MNRAS, 451, 4311
Riaz, B., Gizis, J. E., & Harvin, J. 2006, AJ, 132, 866
Rickard, J. J., & Cronyn, W. M. 1979, ApJ, 228, 755
Sebastian, D., Gillon, M., Ducrot, E., et al. 2021, A&A, 645, A100
Sekhar, S., Jagannathan, P., Kirk, B., Bhatnagar, S., & Taylor, R. 2022, AJ,
   163, 87
Sengar, R., Bailes, M., Balakrishnan, V., et al. 2023, MNRAS, 522, 1071
Sett, S., Bhat, N. D. R., Sokolowski, M., & Lenc, E. 2023, PASA, 40, e003
Smith, D. A., Abdollahi, S., Ajello, M., et al. 2023, ApJ, 958, 191
Sobey, C., Bassa, C. G., O'Sullivan, S. P., et al. 2022, A&A, 661, A87
Sobey, C., Johnston, S., Dai, S., et al. 2021, MNRAS, 504, 228
Song, D., Eckner, C., Gordon, C., et al. 2024, MNRAS, 530, 4395
Stassun, K. G., Oelkers, R. J., Paegert, M., et al. 2019, AJ, 158, 138
Strom, R. G. 1987, ApJL, 319, L103
Tapia, M., Rodríguez, L. F., Tovmassian, G., et al. 2014, RMxAA, 50, 127
Taylor, A. R., Sekhar, S., Heino, L., et al. 2024, MNRAS, 528, 2511
Taylor, M., 2011 TOPCAT: Tool for OPerations on Catalogues And Tables,
   Astrophysics Source Code Library, ascl:1101.010
Taylor, M. B. 2005, in ASP Conf. Ser. 347, Astronomical Data Analysis
   Software and Systems XIV, ed. P. Shopbell, M. Britton, & R. Ebert (San
   Francisco, CA: ASP), 29
```

Intema, H. T., Jagannathan, P., Mooley, K. P., & Frail, D. A. 2017, A&A,

Urquhart, R., Bahramian, A., Strader, J., et al. 2020, ApJ, 904, 147 van der Velden, E. 2020, JOSS, 5, 2004 van Straten, W., & Bailes, M. 2011, PASA, 28, 1 van Straten, W., Demorest, P., & Oslowski, S. 2012, AR&T, 9, 237 Wang, Y., Murphy, T., Kaplan, D. L., et al. 2022a, ApJ, 930, 38 Wang, Z., Kaplan, D. L., Murphy, T., et al. 2021, ApJ, 920, 45 Wang, Z., Kaplan, D. L., Sengar, R., et al. 2024, ApJ, 961, 175 Wang, Z., Murphy, T., Kaplan, D. L., et al. 2022b, MNRAS, 516, 5972 Wenger, M., Ochsenbein, F., Egret, D., et al. 2000, A&AS, 143, 9

White, J. A., Tapia-Vázquez, F., Hughes, A. G., et al. 2021, ApJL, 912, L5 Williams, W. L., Intema, H. T., & Röttgering, H. J. A. 2013, A&A, 549, A55 Wilson, T. J., & Naylor, T. 2018, MNRAS, 481, 2148
Wright, E. L., Eisenhardt, P. R. M., Mainzer, A. K., et al. 2010, AJ, 140, 1868 Yao, J. M., Manchester, R. N., & Wang, N. 2017, ApJ, 835, 29
Zhang, L., Manchester, R. N., Cameron, A. D., et al. 2020, ApJL, 905, L8
Zhao, J.-H., Morris, M. R., & Goss, W. M. 2022, ApJL, 927, L6
Zhao, J.-H., Roberts, D. A., Goss, W. M., et al. 1992, Sci, 255, 1538
Zic, A., Wang, Z., Lenc, E., et al. 2024, MNRAS, 528, 5730